The Astrophysical Journal, 907:64 (20pp), 2021 February 1 https://doi.org/10.3847/1538-4357/abcd9b

Stratified and Vertically Shearing Streaming Instabilities in Protoplanetary Disks

Min-Kai Lin
Institute of Astronomy and Astrophysics, Academia Sinica, Taipei 10617, Taiwan; mklin@asiaa.sinica.edu.tw

Received 2020 September 2; revised 2020 November 3; accepted 2020 November 23; published 2021 January 29

Abstract

Under the right conditions, the streaming instability between imperfectly coupled dust and gas is a powerful mechanism for planetesimal formation as it can concentrate dust grains to the point of gravitational collapse. In its simplest form, the streaming instability can be captured by analyzing the linear stability of unstratified disk models, which represent the midplane of protoplanetary disks. We extend such studies by carrying out vertically global linear stability analyses of dust layers in protoplanetary disks. We find that the dominant form of instability in stratified dust layers is the one driven by the vertical gradient in the rotation velocity of the dust−gas mixture, but also requires partial dust−gas coupling. These vertically shearing streaming instabilities grow on orbital timescales and occur on radial length scales $\sim 10^{-3}H_{\rm g}$, where $H_{\rm g}$ is the local pressure scale height. The classic streaming instability, associated with the relative radial drift between dust and gas, occurs on radial length scales $\sim 10^{-2}H_{\rm g}$, but has much smaller growth rates than vertically shearing streaming instabilities. Including gas viscosity is strongly stabilizing and leads to vertically elongated disturbances. We briefly discuss the potential effects of vertically shearing streaming instabilities on planetesimal formation.

Unified Astronomy Thesaurus concepts: Protoplanetary disks (1300); Hydrodynamics (1963); Astrophysical fluid dynamics (101); Planet formation (1241); Planetesimals (1259)

1. Introduction

The formation of planetesimals from millimeter- to centimeter-sized dust grains or pebbles in protoplanetary disks (PPDs) is a key stage in planet formation (Birnstiel et al. 2016). Neither pairwise collisions nor gravitational forces lead to effective growth on pebble scales (Chiang & Youdin 2010; Blum 2018). However, if a swarm of solids can be made sufficiently dense relative to the ambient gas, then it can undergo direct self-gravitational collapse into kilometer- or larger-sized planetesimals (Goldreich & Ward 1973). The critical dust-to-gas ratio for collapse is $\gg$1 (Shi & Chiang 2013). This should be compared to the typical value of $\sim$1% expected uniformly throughout a newly born PPD (Testi et al. 2014). Thus, an efficient mechanism is needed to first concentrate dust grains. These include dust settling, particle, trapping by pressure bumps, and dust−gas instabilities (Johansen et al. 2014).

The streaming instability (SI; Youdin & Goodman 2005; Youdin & Lithwick 2007) is one such candidate. The SI is a linear instability in rotating flows of partially coupled dust and gas that mutually interact through frictional drag—conditions natural in PPDs—which can amplify dust-to-gas ratios by orders of magnitude and trigger gravitational collapse (Johansen et al. 2009), although the SI itself does not require self-gravity. In the often considered, idealized case of a laminar disk with a monodisperse dust population, the SI is a robust process and has thus received considerable attention as the de facto mechanism for planetesimal formation.

The SI has undergone intense studies through numerical simulations (Johansen & Youdin 2007; Bai & Stone 2010a; Yang & Johansen 2014; Yang et al. 2017). Modern simulations have generalized the SI to consider magnetic fields (Balsara et al. 2009; Tilley et al. 2010; Yang et al. 2018), various geometries (Kowalik et al. 2013; Schreiber & Klahr 2018), multiple grain sizes (Bai & Stone 2010b, 2010c; Schaffer et al. 2018; Benítez-Llambay et al. 2019; Krapp et al. 2019; Zhu & Yang 2020), turbulence (Gole et al. 2020; Schäfer et al. 2020), self-gravity (Simon et al. 2016; Schäfer et al. 2017; Li et al. 2019), pressure bumps (Carrera et al. 2020), etc. These efforts are necessary to understand planetesimal formation in realistic PPDs. Indeed, sophisticated simulations show that planetesimals formed through the SI have properties consistent with those in the solar system (Nesvorný et al. 2019).

On the other hand, a physical understanding of the SI through analytical studies has progressed more slowly. Jacquet et al. (2011) showed that the SI is driven by a process of runaway dust-trapping by pressure bumps, while Lin & Youdin (2017) gave a thermodynamic interpretation of the SI in which partial dust−gas coupling leads to "PdV" work that acts to amplify oscillations.

Recently, Squire & Hopkins (2020) presented detailed models of Youdin & Goodman's (2005) classic SI, in which the mutual interaction between epicyclic motions and the relative radial dust−gas drift in a PPD leads to growing perturbations. In fact, for small dust-to-gas ratios, the classic SI belongs to a broader class of "resonant drag instabilities" (RDIs; Squire & Hopkins 2018a, 2018b; Zhuravlev 2019) generic to dusty gas in which the relative dust−gas motions resonate with a wave mode in the gas. The classic SI is thus expected in PPDs as dust and gas naturally exhibit a relative radial drift, as the gas rotation is partially supported by a (negative) radial pressure gradient (Whipple 1972; Weidenschilling 1977).

The classic SI can be captured in relatively simple disk models, such as those employed by Youdin & Goodman, who considered a small region near the disk midplane. In this limit, the vertical gravity from the central star can be ignored, which produces a uniform vertical disk structure. These "unstratified" disk models allow significant simplifications for analyses of the linear SI and generalizations thereof, which include the effect of pressure bumps, multiple species, and turbulence (Auffinger & Laibe 2018; Krapp et al. 2019; Chen & Lin 2020; Jaupart & Laibe 2020; Paardekooper et al. 2020; Pan 2020; Umurhan et al. 2020).

However, PPDs do have a vertical structure. Dust settling, which leads to the formation of a dense particle layer about the disk midplane (Dubrulle et al. 1995), is often considered as a prerequisite to trigger the SI, as it requires dust-to-gas ratios of order unity or above to operate efficiently (Youdin & Goodman 2005). Dust settling naturally produces a stratified dust layer. In fact, stratified simulations are now common, but the linear SI has not been examined in stratified disks. Filling this gap will be helpful in understanding how the SI operates in realistic PPDs.

The purpose of this work is to generalize previous studies of the linear SI to account for the vertical structure of dust layers in PPDs. To this end, we analyze the stability of vertically global, radially local models of dusty disks. We employ the standard, two-fluid description of dusty gas, as well as a simplified "one-fluid" model (Lin & Youdin 2017) to verify some of our calculations.

Our main result is that in stratified disks, the vertical variation in the azimuthal velocity of the dusty gas (or vertical shear) provides a significant source of "free energy" that can be accessed by partial dust−gas coupling, which results in instability. We typically find that these vertically shearing streaming instabilities (VSSIs) dominate over classic SIs, so the former should be the first to develop in settled dust layers. Our study confirms and expands upon an earlier work from Ishitsu et al. (2009), who used direct simulations to study the effect of vertical dust density gradients on the evolution of dust layers.

This paper is organized as follows. By way of introducing notation, we first provide order-of-magnitude motivations to examine the SI in stratified disks in Section 2. We then describe our framework and disk models in Section 3. Results from our linear stability analyses are presented in Section 5 for three examples: a high dust density layer, a low dust density layer, and a viscous disk. We discuss the implications of our findings in Section 6 and conclude in Section 7. A list of frequently used symbols is summarized in Appendix A.

2. Physical Motivation

2.1. Geometric Considerations

The classic SI of Youdin & Goodman (2005), discovered in unstratified disk models, is driven by the relative radial drift between dust and gas,

$$v_{\mathrm{drift}} = -\frac{2\mathrm{St}(1+\epsilon)\eta r\Omega}{\mathrm{St}^2 + (1+\epsilon)^2} \tag{1}$$

(Nakagawa et al. 1986), where the Stokes number St is a dimensionless inverse measure of the strength of the dust−gas coupling (and is proportional to the grain size), ϵ is the dust-to-gas volume density ratio, r is the cylindrical distance from the star, $\Omega = \sqrt{GM_*/r^3}$ is the Keplerian frequency (M_* and G being the stellar mass and gravitational constant, respectively), and η is a dimensionless measure of the global radial pressure gradient defined as

$$\eta \equiv -\frac{1}{2r\Omega^2\rho_{\mathrm{g}}}\frac{\partial P}{\partial r}, \tag{2}$$

where ρ_{g} is the gas density and P is the gas pressure. PPDs have $\eta \sim O(h_{\mathrm{g}}^2)$, where $h_{\mathrm{g}} \equiv H_{\mathrm{g}}/r$ is the gas disk aspect ratio and H_{g} is the pressure scale height, with $h_{\mathrm{g}} \sim 0.05$.

We thus expect the SI to have characteristic length scales $\sim \eta r$, which is significantly shorter than the global radial length scales of typical PPD disk models ($\sim r$). The SI can thus be considered as a radially localized phenomenon. However, the situation differs in the vertical direction.

In realistic PPDs, dust settles into a layer of thickness H_{d}, which can be related to the midplane dust-to-gas mass density ratio ϵ_0 and the metallicity

$$Z \equiv \frac{\Sigma_{\mathrm{d}}}{\Sigma_{\mathrm{g}}} \simeq \epsilon_0\frac{H_{\mathrm{d}}}{H_{\mathrm{g}}} \tag{3}$$

(Johansen et al. 2014), where $\Sigma_{\mathrm{d,g}}$ are the dust and gas surface densities, respectively. The SI operates on dynamical timescales when $\epsilon_0 \gtrsim 1$ (Youdin & Goodman 2005). To meet this condition at standard solar solid abundances of $Z \simeq 0.01$, dust layers should be thin, $H_{\mathrm{d}} \simeq 0.01H_{\mathrm{g}}$. For an SI mode with vertical length scale ηr to exist, it should fit inside the dust layer, or

$$\chi \equiv \frac{\eta r}{H_{\mathrm{d}}} = \hat{\eta}\left(\frac{\epsilon_0}{Z}\right) \lesssim 1, \tag{4}$$

where $\hat{\eta} \equiv \eta/h_{\mathrm{g}}$ and PPDs typically have $\hat{\eta} \simeq 0.05$.

For a settled dust layer with $\epsilon_0 \simeq 1$ in a disk with standard metallicity $Z \simeq 0.01$, we find $\chi \simeq 5$, violating the above condition. Moreover, when gas viscosity and particle diffusion are considered, SI modes have vertical length scales comparable to H_{g} (Umurhan et al. 2020), while further restricting vertical length scales to $\lesssim H_{\mathrm{d}}$ results in negligible growth rates (Chen & Lin 2020). These findings call for stratified analyses.

2.2. Energetic Considerations

Dusty PPDs possess vertical shear: the settled, dust-rich midplane rotates closer to the Keplerian speed $r\Omega$ than the gas-dominated, pressure-supported disk away from the dust layer, which has a sub-Keplerian rotation of $(1-\eta)r\Omega$ because $\eta > 0$ usually. Such a vertical variation of the disk's rotation speed is an important source of free energy (as borne out in our calculations).

Now, the difference in the azimuthal velocity of the dusty midplane and the overlying gas is $\Delta v_\phi \sim \eta r\Omega$. For a dust layer thickness H_{d}, we can thus estimate the vertical shear rate within the layer as $\eta r\Omega/H_{\mathrm{d}} = \chi\Omega$. For small grains, this vertical shear rate is larger than the relative radial drift rate $v_{\mathrm{drift}}/\eta r$ by a factor of $\mathrm{St}^{-1} \gg 1$.

We can also compare vertical shear to the vertical settling of grains, as the latter can trigger a "dust-settling instability" (DSI; Squire & Hopkins 2018b; Krapp et al. 2020). Taking the typical settling speed of a dust grain to be $|v_{\mathrm{dz}}| \sim \mathrm{St}H_{\mathrm{d}}\Omega$ (Takeuchi & Lin 2002), we find $|\Delta v_\phi/v_{\mathrm{dz}}| \sim \hat{\eta}\epsilon_0/(\mathrm{St}Z)$. For PPDs, with $\epsilon_0 \sim 1$ and $\hat{\eta} \sim Z \sim O(10^{-2})$, this ratio is $\sim \mathrm{St}^{-1}$, i.e., large for small grains.

The above estimates suggest that for small grains, vertical shear is a much larger energy source than the relative radial drift or dust settling. Indeed, in the limit of $\mathrm{St} \to 0$, the classic SI and DSI are suppressed and vertical shear drives nonaxisymmetric Kelvin–Helmholtz instabilities (KHIs; Chiang 2008; Lee et al. 2010).

In this work, we consider axisymmetric disturbances so that KHIs are not applicable. Lin & Youdin (2017) showed that axisymmetric dusty disks are generally stable in the limit $\mathrm{St} \to 0$, however large the vertical shear rate. This is due to stabilization by dust-induced, effective buoyancy forces (see also Lin 2019).

However, the above result ceases to be valid for $\mathrm{St} \neq 0$, because in this case, dust and gas are no longer perfectly coupled, and they can stream past one another, which diminishes the stabilizing effect of dusty buoyancy. This is similar to how rapid cooling can enable the "vertical shear instability" (VSI) in gaseous PPDs (Nelson et al. 2013; Lin & Youdin 2015) by eliminating gas buoyancy. (For the gaseous VSI, vertical shear originates from the disk's radial thermal structure.)

We can therefore expect in a stratified, dusty disk the free energy associated with vertical shear, here a result of dust settling, to be accessible through an instability with nonvanishing particle sizes. Indeed, we will find such instabilities are the dominant modes in stratified disks. We refer to them as VSSIs, because both vertical shear and dust–gas streaming motions are necessary.

3. Basic Equations

We consider a non-self-gravitating, unmagnetized PPD comprising gas and a single species of dust grains around a central star of mass M_*. The gas component has density, pressure, and velocity fields $(\rho_\mathrm{g}, P, \boldsymbol{V}_\mathrm{g})$. We assume an isothermal gas so that $P = c_s^2 \rho_\mathrm{g}$ with a constant sound speed $c_s = H_\mathrm{g}\Omega$.

We treat the dust population as a pressureless fluid with density and velocity $(\rho_\mathrm{d}, \boldsymbol{V}_\mathrm{d})$. The dust and gas fluids interact via a drag force parameterized by a stopping time τ_s (see below). The fluid approximation for dust is then valid for well-coupled, small grains such that $\tau_\mathrm{s} \lesssim \Omega^{-1}$ (Jacquet et al. 2011).

3.1. Two-fluid, Radially Local, Axisymmetric Disk Model

We study radially localized disturbances in the aforementioned dusty disk using the shearing box framework (Goldreich & Lynden-Bell 1965). The shearing box is centered about a fiducial point $(r_0, \phi_0, 0)$ in cylindrical coordinates on the star, which rotates at the reference Keplerian frequency $\Omega(r_0) \equiv \Omega_0$, i.e., $\phi_0 = \Omega_0 t$. Cartesian coordinates (x, y, z) in the box correspond to the radial, azimuthal, and vertical directions in the global disk. The radial extent of the box is assumed to be much smaller than r_0, so that curvature terms from the cylindrical geometry can be ignored. Keplerian rotation is then approximated as the linear shear flow $-(3/2)\Omega_0 x\hat{\boldsymbol{y}}$. We define $\boldsymbol{v}_\mathrm{d,g} \equiv \boldsymbol{V}_\mathrm{d,g} - (r_0 - 3x/2)\Omega_0\hat{\boldsymbol{y}}$ as the local dust and gas velocities in the shearing box relative to this linear shear flow. We assume axisymmetry throughout, so that $\partial_y \equiv 0$.

The governing equations for the dust component in the shearing box are

$$\frac{\partial \rho_\mathrm{d}}{\partial t} + \nabla \cdot (\rho_\mathrm{d} \boldsymbol{v}_\mathrm{d}) = \nabla \cdot \left[D\rho_\mathrm{g} \nabla \left(\frac{\rho_\mathrm{d}}{\rho_\mathrm{g}} \right) \right], \tag{5}$$

$$\frac{\partial \boldsymbol{v}_\mathrm{d}}{\partial t} + \boldsymbol{v}_\mathrm{d} \cdot \nabla \boldsymbol{v}_\mathrm{d} = 2\Omega_0 v_{\mathrm{d}y}\hat{\boldsymbol{x}} - \frac{\Omega_0}{2} v_{\mathrm{d}x}\hat{\boldsymbol{y}} - \Omega_0^2 z\hat{\boldsymbol{z}} - \frac{1}{\tau_\mathrm{s}}(\boldsymbol{v}_\mathrm{d} - \boldsymbol{v}_\mathrm{g}), \tag{6}$$

where D is a constant diffusion coefficient defined below. The third term on the right-hand side (rhs) of Equation (6) corresponds to the vertical component of the stellar gravity in the thin-disk limit. The last term on the rhs corresponds to gas drag, the strength of which is characterized by the stopping time τ_s.

For the gas, we include the effect of a global radial pressure gradient in the shearing box by writing

$$\nabla P \to \nabla P - 2\eta_0 r_0 \Omega_0^2 \rho_\mathrm{g} \hat{\boldsymbol{x}}, \tag{7}$$

where $\eta_0 = \eta(r = r_0, z = 0)$ and η is defined by Equation (2). That is, the global radial pressure gradient is modeled as a constant forcing. We then reinterpret P as pressure fluctuations in the shearing box. The governing equations for the gas component are then

$$\frac{\partial \rho_\mathrm{g}}{\partial t} + \nabla \cdot (\rho_\mathrm{g} \boldsymbol{v}_\mathrm{g}) = 0, \tag{8}$$

$$\begin{aligned}\frac{\partial \boldsymbol{v}_\mathrm{g}}{\partial t} + \boldsymbol{v}_\mathrm{g} \cdot \nabla \boldsymbol{v}_\mathrm{g} = 2\Omega_0 v_{\mathrm{g}y}\hat{\boldsymbol{x}} - \frac{\Omega_0}{2} v_{\mathrm{g}x}\hat{\boldsymbol{y}} - \frac{\nabla P}{\rho_\mathrm{g}} \\ + 2\eta_0 \Omega_0^2 r_0 \hat{\boldsymbol{x}} + \frac{1}{\rho_\mathrm{g}} \nabla \cdot \boldsymbol{T} \\ - \Omega_0^2 z\hat{\boldsymbol{z}} - \frac{\epsilon}{\tau_\mathrm{s}}(\boldsymbol{v}_\mathrm{g} - \boldsymbol{v}_\mathrm{d}).\end{aligned} \tag{9}$$

The fifth term on the rhs of Equation (9) represent viscous forces, where

$$\boldsymbol{T} = \rho_\mathrm{g} \nu \left[\nabla \boldsymbol{v}_\mathrm{g} + (\nabla \boldsymbol{v}_\mathrm{g})^\dagger - \frac{2}{3} \boldsymbol{I} \nabla \cdot \boldsymbol{v}_\mathrm{g} \right] \tag{10}$$

is the viscous stress tensor and ν is a kinematic viscosity, prescribed later. The final term on the rhs is the back-reaction of dust drag onto the gas.

The basic Equations (5)–(6) and (8)–(9) extend those used by Chen & Lin (2020) with the addition of vertical gravity, which themselves are extensions of those in Youdin & Johansen (2007) with the addition of dust diffusion and gas viscosity. We solve Equations (5)–(6) and (8)–(9) in full to obtain equilibrium states, then solve their linearized versions to study the stability of said equilibria. Both problems are one dimensional in z. For numerical solutions, we consider the half-disk $z \in [0, z_\mathrm{max}]$ by imposing symmetry conditions at the midplane. Details are given in Sections 3.5.1–3.5.2 and Section 4. Hereafter, we drop the subscript "0" for clarity. Below, H_g refers to the pressure scale height at the reference radius.

3.2. Dust–Gas Drag

The stopping time τ_s is the timescale for a dust particle to reach velocity equilibrium with its surrounding gas. In this work, we take τ_s to be a constant parameter for simplicity. It is convenient to define the dimensionless stopping time or Stokes number,

$$\mathrm{St} = \tau_\mathrm{s}\Omega. \tag{11}$$

We consider well-coupled, or small dust grains with $\mathrm{St} \ll 1$.

Physically, St depends on the particle and gas properties, such as grain size (a), internal density ($\rho_\bullet$), and gas density (Weidenschilling 1977). To put our calculations in context, consider grains in the Epstein regime in a minimum-mass solar-nebula-like (MMSN) disk described in Chiang & Youdin (2010).

We then find

$$\mathrm{St} = 0.019F^{-1}\left(\frac{r}{30\ \mathrm{au}}\right)^{3/2}\left(\frac{\rho_\bullet}{\mathrm{g\ cm^{-3}}}\right)\left(\frac{a}{\mathrm{mm}}\right), \tag{12}$$

where F is a mass scale relative to the standard MMSN ($F = 1$). We are mostly interested in millimeter- or submillimeter-sized grains with internal density 1 g cm^{-3} at tens of astronomical units in MMSN-like disks.

3.3. Dust Diffusion

We include dust diffusion to allow a stratified equilibrium state to be defined, in which dust settling is balanced by dust diffusion. Without dust diffusion, particles would continuously settle and no steady state can be established for standard stability analyses. Dust diffusion is usually attributed to gas turbulence (e.g., Youdin & Lithwick 2007; Laibe et al. 2020), which is often modeled as gas viscosity. We thus parameterize dust diffusion in terms of a gas viscosity, although for the most part we ignore viscosity in the gas equations.

We model dust diffusion via the constant parameter δ such that

$$D = \delta c_s H_g, \tag{13}$$

with δ given by

$$\delta = \frac{1 + \mathrm{St} + 4\mathrm{St}^2}{(1 + \mathrm{St}^2)^2}\alpha \tag{14}$$

(Youdin & Lithwick 2007; Youdin 2011), where α is an input constant turbulent viscosity parameter defined below. In practice, $\delta \simeq \alpha$ because we consider small grains.

3.4. Turbulent Viscosity

When considered, we model gas turbulence via a viscous stress tensor (see Equation (10)) and adopt the standard alpha prescription (Shakura & Sunyaev 1973) such that the kinematic viscosity is

$$\nu = \alpha c_s H_g \frac{\rho_{g,\mathrm{eqm}}}{\rho_g}, \tag{15}$$

where $\rho_{g,\mathrm{eqm}}(z)$ denotes the equilibrium gas density, derived below. We use this prescription so that the dynamic viscosity $\rho_g \nu$ is a fixed function of space, which avoids viscous overstabilities that could complicate results (Latter & Ogilvie 2006; Lin & Kratter 2016).

3.5. Two-fluid Equilibria

We seek steady, horizontally uniform equilibria with $\partial_t = \partial_x = 0$. The gas continuity equation then implies $v_{gz} = 0$. All other are quantities are nonzero and z dependent, e.g., $\rho_g = \rho_{g,\mathrm{eqm}}(z)$. For clarity, hereafter we drop the subscript "eqm" on the equilibrium fields.

3.5.1. Vertical Equilibrium

The equilibrium dust mass and vertical momentum equations are

$$\frac{d\ln\epsilon}{dz} = \frac{v_{dz}}{D}, \tag{16}$$

$$c_s^2\frac{d\ln\rho_g}{dz} = \frac{\epsilon\Omega}{\mathrm{St}}v_{dz} - \Omega^2 z, \tag{17}$$

$$v_{dz}\frac{dv_{dz}}{dz} = -\Omega^2 z - \frac{\Omega}{\mathrm{St}}v_{dz}, \tag{18}$$

where we recall $\epsilon = \rho_d/\rho_g$. For constant St, these may be solved exactly to yield

$$\epsilon(z) = \epsilon_0 \exp\left(-\frac{\beta}{2\delta}\frac{z^2}{H_g^2}\right), \tag{19}$$

$$\rho_g(z) = \rho_{g0}\exp\left[\frac{\delta}{\mathrm{St}}(\epsilon - \epsilon_0) - \frac{z^2}{2H_g^2}\right], \tag{20}$$

$$v_{dz}(z) = -\beta z\Omega, \tag{21}$$

where ϵ_0, ρ_{g0} is the midplane dust-to-gas ratio and gas density, respectively, and

$$\beta \equiv \frac{1}{2\mathrm{St}}\left(1 - \sqrt{1 - 4\mathrm{St}^2}\right). \tag{22}$$

We thus require $\mathrm{St} \leqslant 0.5$. Note that $\beta \simeq \mathrm{St}$[1] for the small particles considered in this work ($\mathrm{St} \ll 1$). We also consider weak diffusion such that $\delta \ll \mathrm{St}$. The dust layer thickness can then be approximated by

$$H_d = \sqrt{\frac{\delta}{\delta + \mathrm{St}}}H_g \tag{23}$$

(Dubrulle et al. 1995; Zhu et al. 2015). The local metallicity is

$$Z \equiv \frac{\int_{-\infty}^{\infty}\rho_d dz}{\int_{-\infty}^{\infty}\rho_g dz} = \frac{\Sigma_d}{\Sigma_g}. \tag{24}$$

In practice, we adjust ϵ_0 until a specified value of Z is obtained. However, Equations (3) and (23) also give an adequate estimate, $\epsilon_0 \simeq Z\sqrt{\mathrm{St}/\delta}$. The vertical structure is then completely determined.

3.5.2. Horizontal Equilibrium

The equilibrium horizontal momentum equations are

$$v_{dz}\frac{dv_{dx}}{dz} = 2\Omega v_{dy} - \frac{\Omega}{\mathrm{St}}(v_{dx} - v_{gx}), \tag{25}$$

$$v_{dz}\frac{dv_{dy}}{dz} = -\frac{\Omega}{2}v_{dx} - \frac{\Omega}{\mathrm{St}}(v_{dy} - v_{gy}), \tag{26}$$

$$0 = 2\Omega v_{gy} + 2\eta\Omega^2 r - \frac{\epsilon\Omega}{\mathrm{St}}(v_{gx} - v_{dx}) + \frac{\nu}{\rho_g}\frac{d}{dz}\left(\rho_g\frac{dv_{gx}}{dz}\right), \tag{27}$$

$$0 = -\frac{\Omega}{2}v_{gx} - \frac{\epsilon\Omega}{\mathrm{St}}(v_{gy} - v_{dy}) + \frac{\nu}{\rho_g}\frac{d}{dz}\left(\rho_g\frac{dv_{gy}}{dz}\right), \tag{28}$$

with $\epsilon(z)$, $\rho_g(z)$, and $v_{dz}(z)$ given by Equations (19)–(21). The horizontal velocity profiles must, in general, be solved numerically subject to appropriate boundary conditions. However, for $|z| \to \infty$ and thus $\epsilon \to 0$, the dust and gas equations

---

[1] This can been seen by performing a Taylor expansion of the numerator in Equation (22).

decouple, and we obtain

$$\lim_{\epsilon\to 0} v_{\mathrm{d}x} = -\frac{2\mathrm{St}\eta r\Omega}{1+\mathrm{St}^2}, \tag{29}$$

$$\lim_{\epsilon\to 0} v_{\mathrm{d}y} = -\frac{\eta r\Omega}{1+\mathrm{St}^2}, \tag{30}$$

$$\lim_{\epsilon\to 0} v_{\mathrm{g}x} = 0, \tag{31}$$

$$\lim_{\epsilon\to 0} v_{\mathrm{g}y} = -\eta r\Omega, \tag{32}$$

which are constants. These correspond to a sub-Keplerian gas flow that does not feel the dust drag, while the dust drifts inwards in response to gas drag. Equations (29)–(32) are consistent with the unstratified solutions of Nakagawa et al. (1986).

When gas viscosity is ignored, we impose Equations (29) and (30) at a finite height $z = z_{\max}$ such that $\epsilon \ll 1$. When gas viscosity is included, we impose Equations (29)–(32) at $z = z_{\max}$, as well as $v'_{\mathrm{g}x}(0) = v'_{\mathrm{g}y}(0) = 0$, where $'$ denotes d/dz.

3.6. One-fluid Models

We also employ the "one-fluid" description of dusty gas (Laibe & Price 2014; Price & Laibe 2015; Lin & Youdin 2017) to confirm selected results. In this framework, we work with the total mass ρ and the center-of-mass velocity $\boldsymbol{v}_c$ of the dust-plus-gas mixture, which is treated as a single, ideal fluid subject to a special cooling function. This approximation is valid for small particles with $\mathrm{St} \ll 1$. Our one-fluid formulation includes dust diffusion, but without gas viscosity (see Lovascio & Paardekooper 2019). Details are given in Appendix B.

4. Linear Problem

We consider axisymmetric Eulerian perturbations of the form

$$\delta\rho_{\mathrm{g}}(z)\exp(ik_x x + \sigma t), \tag{33}$$

where k_x is a (real) radial wavenumber taken to be positive without loss of generality, and σ is the complex frequency or eigenvalue,

$$\sigma \equiv s - i\omega, \tag{34}$$

where s is the real growth rate and ω is the oscillation frequency. We also refer to the complex amplitudes such as $\delta\rho_{\mathrm{g}}(z)$ and their normalized versions (e.g., $\delta\rho_{\mathrm{g}}/\rho_{\mathrm{g}}$) as the eigenfunctions. The initial perturbation in real space is then obtained by taking $\mathrm{Re}\,[\delta\rho_{\mathrm{g}}\exp(ik_x x)]$. Similar definitions apply to other variables.

The linearized equations for the dust fluid read

$$\begin{aligned}
&\sigma\frac{\delta\rho_{\mathrm{d}}}{\rho_{\mathrm{d}}} + ik_x\left(v_{\mathrm{d}x}\frac{\delta\rho_{\mathrm{d}}}{\rho_{\mathrm{d}}} + \delta v_{\mathrm{d}x}\right) + \frac{\rho'_{\mathrm{d}}}{\rho_{\mathrm{d}}}\left(v_{\mathrm{d}z}\frac{\delta\rho_{\mathrm{d}}}{\rho_{\mathrm{d}}} + \delta v_{\mathrm{d}z}\right)\\
&v_{\mathrm{d}z}\left(\frac{\delta\rho_{\mathrm{d}}}{\rho_{\mathrm{d}}}\right)' + v'_{\mathrm{d}z}\frac{\delta\rho_{\mathrm{d}}}{\rho_{\mathrm{d}}} + \delta v'_{\mathrm{d}z} = -Dk_x^2\frac{\delta\epsilon}{\epsilon}\\
&+\frac{D}{\epsilon}\left[\frac{\rho'_{\mathrm{g}}}{\rho_{\mathrm{g}}}\left(\epsilon'\frac{\delta\rho_{\mathrm{g}}}{\rho_{\mathrm{g}}} + \delta\epsilon'\right) + \epsilon''\frac{\delta\rho_{\mathrm{g}}}{\rho_{\mathrm{g}}} + \epsilon'\left(\frac{\delta\rho_{\mathrm{g}}}{\rho_{\mathrm{g}}}\right)' + \delta\epsilon''\right],
\end{aligned} \tag{35}$$

$$\begin{aligned}
&\sigma\delta v_{\mathrm{d}x} + ik_x v_{\mathrm{d}x}\delta v_{\mathrm{d}x} + v'_{\mathrm{d}x}\delta v_{\mathrm{d}z} + v_{\mathrm{d}z}\delta v'_{\mathrm{d}x}\\
&= 2\Omega\delta v_{\mathrm{d}y} - \frac{\Omega}{\mathrm{St}}(\delta v_{\mathrm{d}x} - \delta v_{\mathrm{g}x}),
\end{aligned} \tag{36}$$

$$\begin{aligned}
&\sigma\delta v_{\mathrm{d}y} + ik_x v_{\mathrm{d}x}\delta v_{\mathrm{d}y} + v'_{\mathrm{d}y}\delta v_{\mathrm{d}z} + v_{\mathrm{d}z}\delta v'_{\mathrm{d}y}\\
&= -\frac{\Omega}{2}\delta v_{\mathrm{d}x} - \frac{\Omega}{\mathrm{St}}(\delta v_{\mathrm{d}y} - \delta v_{\mathrm{g}y}),
\end{aligned} \tag{37}$$

$$\begin{aligned}
&\sigma\delta v_{\mathrm{d}z} + ik_x v_{\mathrm{d}x}\delta v_{\mathrm{d}z} + v'_{\mathrm{d}z}\delta v_{\mathrm{d}z} + v_{\mathrm{d}z}\delta v'_{\mathrm{d}z}\\
&= -\frac{\Omega}{\mathrm{St}}(\delta v_{\mathrm{d}z} - \delta v_{\mathrm{g}z}),
\end{aligned} \tag{38}$$

and those for gas are

$$\sigma\frac{\delta\rho_{\mathrm{g}}}{\rho_{\mathrm{g}}} + ik_x\left(v_{\mathrm{g}x}\frac{\delta\rho_{\mathrm{g}}}{\rho_{\mathrm{g}}} + \delta v_{\mathrm{g}x}\right) + \frac{\rho'_{\mathrm{g}}}{\rho_{\mathrm{g}}}\delta v_{\mathrm{g}z} + \delta v'_{\mathrm{g}z} = 0, \tag{39}$$

$$\sigma\delta v_{\mathrm{g}x} + ik_x v_{\mathrm{g}x}\delta v_{\mathrm{g}x} + v'_{\mathrm{g}x}\delta v_{\mathrm{g}z} = 2\Omega\delta v_{\mathrm{g}y} - ik_x c_s^2\frac{\delta\rho_{\mathrm{g}}}{\rho_{\mathrm{g}}} + \delta F_x^{\mathrm{br}} + \delta F_x^{\mathrm{visc}}, \tag{40}$$

$$\sigma\delta v_{\mathrm{g}y} + ik_x v_{\mathrm{g}x}\delta v_{\mathrm{g}y} + v'_{\mathrm{g}y}\delta v_{\mathrm{g}z} = -\frac{\Omega}{2}\delta v_{\mathrm{g}x} + \delta F_y^{\mathrm{br}} + \delta F_y^{\mathrm{visc}}, \tag{41}$$

$$\sigma\delta v_{\mathrm{g}z} + ik_x v_{\mathrm{g}x}\delta v_{\mathrm{g}z} = -c_s^2\left(\frac{\delta\rho_{\mathrm{g}}}{\rho_{\mathrm{g}}}\right)' + \delta F_z^{\mathrm{br}} + \delta F_z^{\mathrm{visc}}, \tag{42}$$

where the linearized back-reaction force is

$$\delta\boldsymbol{F}^{\mathrm{br}} \equiv -\frac{\epsilon\Omega}{\mathrm{St}}\left[(\boldsymbol{v}_{\mathrm{g}} - \boldsymbol{v}_{\mathrm{d}})\frac{\delta\epsilon}{\epsilon} + (\delta\boldsymbol{v}_{\mathrm{g}} - \delta\boldsymbol{v}_{\mathrm{d}})\right], \tag{43}$$

and the components of the linearized viscous forces are

$$\begin{aligned}
\delta F_x^{\mathrm{visc}} = \nu\Bigg[&\delta v''_{\mathrm{g}x} - \frac{4}{3}k_x^2\delta v_{\mathrm{g}x} + \frac{1}{3}ik_x\delta v'_{\mathrm{g}z}\\
&+ \frac{\rho'_{\mathrm{g}}}{\rho_{\mathrm{g}}}(\delta v'_{\mathrm{g}x} + ik_x\delta v_{\mathrm{g}z})\Bigg]\\
&- \nu\left(v''_{\mathrm{g}x} + \frac{\rho'_{\mathrm{g}}}{\rho_{\mathrm{g}}}v'_{\mathrm{g}x}\right)\frac{\delta\rho_{\mathrm{g}}}{\rho_{\mathrm{g}}},
\end{aligned} \tag{44}$$

$$\begin{aligned}
\delta F_y^{\mathrm{visc}} = \nu&\left[\delta v''_{\mathrm{g}y} + \frac{\rho'_{\mathrm{g}}}{\rho_{\mathrm{g}}}\delta v'_{\mathrm{g}y} - k_x^2\delta v_{\mathrm{g}y}\right]\\
&- \nu\left(v''_{\mathrm{g}y} + \frac{\rho'_{\mathrm{g}}}{\rho_{\mathrm{g}}}v'_{\mathrm{g}y}\right)\frac{\delta\rho_{\mathrm{g}}}{\rho_{\mathrm{g}}},
\end{aligned} \tag{45}$$

$$\begin{aligned}
\delta F_z^{\mathrm{visc}} = \nu\Bigg[&\frac{4}{3}\delta v''_{\mathrm{g}z} - k_x^2\delta v_{\mathrm{g}z} + \frac{1}{3}ik_x\delta v'_{\mathrm{g}x}\\
&+ \frac{\rho'_{\mathrm{g}}}{\rho_{\mathrm{g}}}\left(\frac{4}{3}\delta v'_{\mathrm{g}z} - \frac{2}{3}ik_x\delta v_{\mathrm{g}x}\right)\Bigg]
\end{aligned} \tag{46}$$

(Lin & Kratter 2016). We remark that one can differentiate the gas continuity Equation (39) to eliminate $\delta v''_{\mathrm{g}z}$ from the expression of $\delta F_z^{\mathrm{visc}}$.

In practice, we solve for the perturbation to the dust-to-gas ratio instead of the dust density perturbation, which are related by

$$\frac{\delta\rho_{\rm d}}{\rho_{\rm d}} = \frac{\delta\epsilon}{\epsilon} + \frac{\delta\rho_{\rm g}}{\rho_{\rm g}} \equiv Q + W. \tag{47}$$

Note that for strictly isothermal gas, we have $W \equiv \delta\rho_{\rm g}/\rho_{\rm g} = \delta P/P$.

The linearized equations may be written in the form

$$\mathcal{L}\boldsymbol{g} = \sigma\boldsymbol{g}, \tag{48}$$

where $\mathcal{L}$ is an 8×8 matrix of linear differential operators and $\boldsymbol{g} = [W, \delta\boldsymbol{v}_{\rm g}, Q, \delta\boldsymbol{v}_{\rm d}]^{\dagger}$. When supplemented with appropriate boundary conditions (see below), this constitutes an eigenvalue problem for $\mathcal{L}$.

4.1. Boundary Conditions

We consider modes symmetric about the midplane such that

$$W'(0) = Q'(0) = \delta v_{{\rm c}x}'(0) = \delta v_{{\rm c}y}'(0) = \delta v_{{\rm c}z}(0) = 0, \tag{49}$$

where $\boldsymbol{v}_{\rm c}$ is the center-of-mass velocity; see Equation (B2). At the top boundary, we impose

$$W'(z_{\max}) = Q(z_{\max}) = 0. \tag{50}$$

When gas viscosity is included, we additionally impose

$$\delta v_{{\rm g}x}'(0) = \delta v_{{\rm g}y}'(0) = \delta v_{{\rm g}x}'(z_{\max}) = \delta v_{{\rm g}y}'(z_{\max}) = 0. \tag{51}$$

We generally find that dominant modes have amplitudes that maximize off the disk midplane and decay toward the domain boundaries, as found by Ishitsu et al. (2009) in direct simulations. As such, boundary conditions are unlikely to modify our main findings.

4.2. Numerical Method

We use DEDALUS (Burns et al. 2020), a general-purpose spectral code for solving partial differential equations, including the linear eigenvalue problem described above. The eigenfunctions are expanded in Chebyshev polynomials T_n up to order $n = N - 1$, and the domain is discretized into N points corresponding to the roots of T_N. Unless otherwise stated, we take $z_{\max} \simeq 5H_{\rm d}$.

We use $N = 1024$ to compute the background disk structure[2] and $N = 384$ for the linearized equations. For the latter, DEDALUS transforms Equation (48) into a generalized matrix eigenvalue problem and solves it via the SciPy package (see Section 9D of Burns et al. 2020). This directly yields the eigenvalues σ and the associated eigenfunctions.

For the eigenvalue problem, we also use the EIGENTOOLS[3] package to filter out spurious numerical solutions due to the discretization. This is done by comparing eigenvalues obtained from different vertical resolutions and only keeping those within some tolerance (here 10^{-6}), i.e., only physical solutions that converge with respect to N_z are kept. See Barker & Latter (2015) for a similar treatment. We also filter out unphysical solutions with large growth rates compared to Ω (Lin & Youdin 2015).

Example source codes for used this work may be obtained from the author's GitHub repository.[4]

4.3. Units and Notation

We use normalized units such that $c_{\rm s} = H_{\rm g} = \Omega = 1$ and quote the dimensionless radial wavenumber $K_x \equiv k_x H_{\rm g}$. It turns out that only the reduced pressure-gradient parameter $\hat{\eta} = \eta r/H_{\rm g}$ is relevant. Eigenfunctions are normalized such that $\delta\rho_{\rm d}/\rho_{\rm d} = 1$ at its maximum amplitude. For clarity, in plot labels we drop the subscripts "d," "g," and "c" when collectively referring to the dust, gas, and center-of-mass velocity fields, respectively.

We quote δ to distinguish models in which only dust diffusion is included, from models wherein corresponding viscous terms are also included in the gas momentum equations, in which case we quote α.

5. Results

We present results for a high dust density layer (Section 5.1), a low dust density layer (Section 5.2), and a viscous disk (Section 5.3). For a given set of disk parameters and K_x, solving the linearized equations accounts for all vertical structures permitted by the boundary conditions and the finite resolution. This can result in a large number of modes. We are interested in unstable modes as they will dominate over decaying ones in a real disk. Thus, solutions with $s < 0$ are discarded, and we focus on those with the largest growth rate $s = s_{\max}$ at a given K_x. Table 1 lists, for each case, approximately[5] the most unstable mode over $10^2 \leqslant K_x \leqslant 10^4$ (based on two-fluid calculations).

5.1. Case A: High Dust Density Layer

We first present a fiducial case with well-settled dust. Here, we ignore gas viscosity but include particle diffusion. This enables a comparison between the two-fluid and one-fluid frameworks, because the latter does not include gas viscosity. We choose $Z = 0.03$, $\hat{\eta} = 0.05$, ${\rm St} = 10^{-2}$, and $\delta \simeq 10^{-6}$. This gives $H_{\rm d} \simeq 0.01H_{\rm g}$. The equilibrium disk profiles are shown in Figure 1.

Figure 2 shows the maximum growth rate and corresponding frequencies for case A for $K_x = 100$–10^4. Growth rates increase with K_x and maximizes around $K_x \sim 3600$. We find two classes of unstable modes: for $K_x \lesssim 200$, the oscillation frequency $\omega \sim \Omega$ and is constant, while for $K_x \gtrsim 200$, oscillation frequencies are negative and increase in magnitude. We find good agreement between the one- and two-fluid results, giving confidence that these are physical solutions.

Example eigenfunctions from the above modes are shown in Figure 3. We find that with increasing K_x, unstable modes become increasingly localized about $z \sim 0.015H_{\rm g}$. Notice that there is little perturbation in the gas density for either mode, which indicate that they are nearly incompressible.

5.1.1. Pseudo-energy Decomposition

In order to identify physical origin of the above instabilities, we follow Ishitsu et al. (2009) and examine the energy-like quantity $U_{\rm tot} = \sum_{i=1}^{6} U_i$ associated with each mode, as described in Appendix C. The contributions U_i include vertical shear in the equilibrium velocity field (U_1, which is dominated

---

[2] In the one-fluid formulation, we use approximate analytic equilibrium solutions; see Appendix B.

[3] https://github.com/DedalusProject/eigentools

[4] https://github.com/minkailin/stratsi

[5] Due to the finite range and sampling in K_x space.

Table 1
Selected Unstable Modes in Stratified Dusty Disks

Case	$\hat{\eta}$	Z	St	$\alpha(\simeq\delta)$	Viscosity[a]	$k_xH_g/10^3$	$s_{\max}/\Omega$	ω/Ω	Comment
A	0.05	0.03	10^{-2}	10^{-6}	no	3.593814	1.155043	−0.8250615	high dust density layer; Figure 2
	0.01	0.03	10^{-2}	10^{-6}	no	5.994843	0.3267454	−0.1839234	smaller pressure gradient; Figure 6
	0.1	0.03	10^{-2}	10^{-6}	no	3.593814	1.724942	−1.858679	larger pressure gradient; Figure 6
	0.05	0.03	10^{-3}	10^{-6}	no	10	0.3901075	−0.05611060	smaller particle; Figure 7
	0.05	0.03	10^{-1}	10^{-6}	no	0.8254042	1.463588	−4.087298	larger particle; Figure 7
	0.05	0.01	10^{-2}	10^{-6}	no	5.994843	0.9145120	−0.4717328	smaller metallicity, Figure 9
	0.05	0.1	10^{-2}	10^{-6}	no	3.593814	1.308362	−1.703580	larger metallicity; Figure 9
B	0.05	0.03	10^{-3}	10^{-5}	no	10	0.06512705	−0.01026995	low dust density layer; Figure 11
C	0.05	0.01	10^{-2}	10^{-7}	yes	1.112355	0.6007165	−0.9712429	viscous disk; Figure 15

Note.
[a] Denotes whether or not viscous terms are included the gas momentum equations.

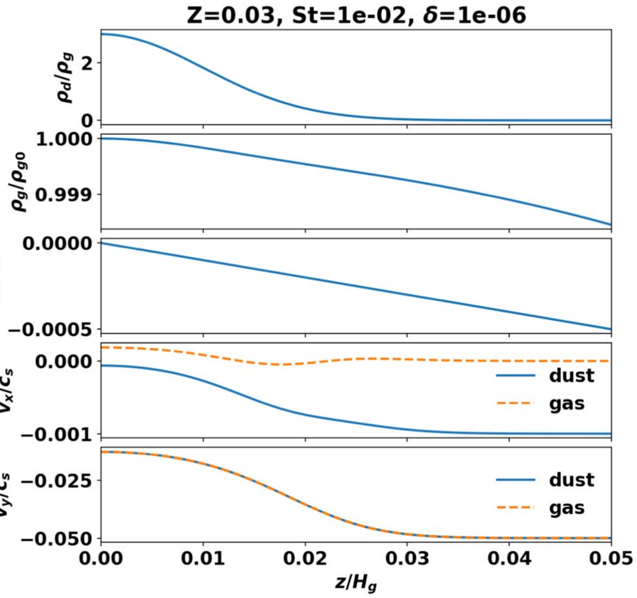

Figure 1. Two-fluid equilibrium for case A with a high dust density layer. From top to bottom: dust-to-gas ratio, gas density, vertical dust velocity, radial velocities, and azimuthal velocities.

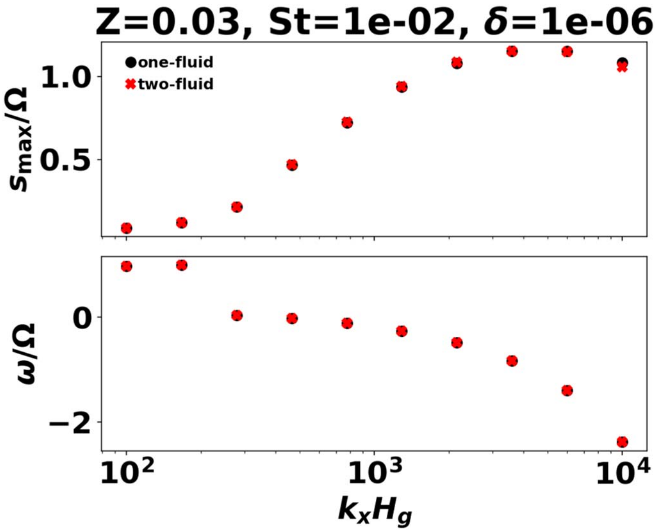

Figure 2. Maximum growth rate (top) and corresponding oscillation frequency (bottom) for unstable modes in case A (high dust density layer), as a function of the dimensionless radial wavenumber K_x.

by the azimuthal component U_{1y}), vertical dust settling (U_2), pressure forces (U_3), dust–gas relative drift (U_4), buoyancy (U_5), and viscosity (U_6). Note that $U_6 \equiv 0$ for inviscid disks, as considered here.

Figure 4 shows the pseudo-energy decomposition of the two main type of modes we find. For $K_x = 100$ the mode is driven by a mixture of relative dust–gas drift (U_4, red), itself dominated by radial drift, and the vertical shear in the azimuthal velocity (U_{1y}, crosses). However, the high $K_x = 3594$ mode is entirely driven by vertical shear.

In Figure 5, we show the vertically integrated pseudo-energy contributions as a function of K_x. We confirm that the abrupt change in oscillation frequencies around $K_x = 200$ (see Figure 2) is due to a change in the character of the most unstable mode. For $K_x \lesssim 250$, modes are destabilized by a combination of dust-gas drift and vertical shear in the azimuthal velocity, while the latter dominates entirely for $K_x \gtrsim 250$. Interestingly, dust–gas drift becomes a stabilizing effect (its contribution becomes negative) for high-K_x modes. On the other hand, vertical shear is always destabilizing.

Figure 5 show that dust settling is always destabilizing, which is consistent with Squire & Hopkins (2018b), who find dust settling alone can lead to instability in vertically local disk models. However, this effect is subdominant in our stratified models because vertical shear is much more significant. We also find that buoyancy forces are always stabilizing, as dust–gas coupling increases the mixture's inertia (Lin & Youdin 2017).

We find pressure forces provide increasing stabilization with increasing K_x, which is expected because pressure acts on small scales. The increased restoring force from pressure may explain the increasing magnitude of oscillation frequencies (Lubow & Pringle 1993; Balbus 2003). Ishitsu et al. (2009) showed that in the limit of an incompressible gas, pressure forces do not contribute to mode growth or decay. This indicates that gas compressibility becomes nonnegligible for the high-K_x modes in our case. These modes have short vertical wavelengths and are localized to regions of largest vertical shear (see Figure 3, right panel). This is reminiscent of "surface modes" of the gaseous VSI (Nelson et al. 2013), which are also stabilized by gas compressibility (McNally & Pessah 2015). These similarities motivate us to interpret the high-K_x, dust-driven, vertical shear modes as dusty analogs of the gaseous VSI; see Section 6.1.

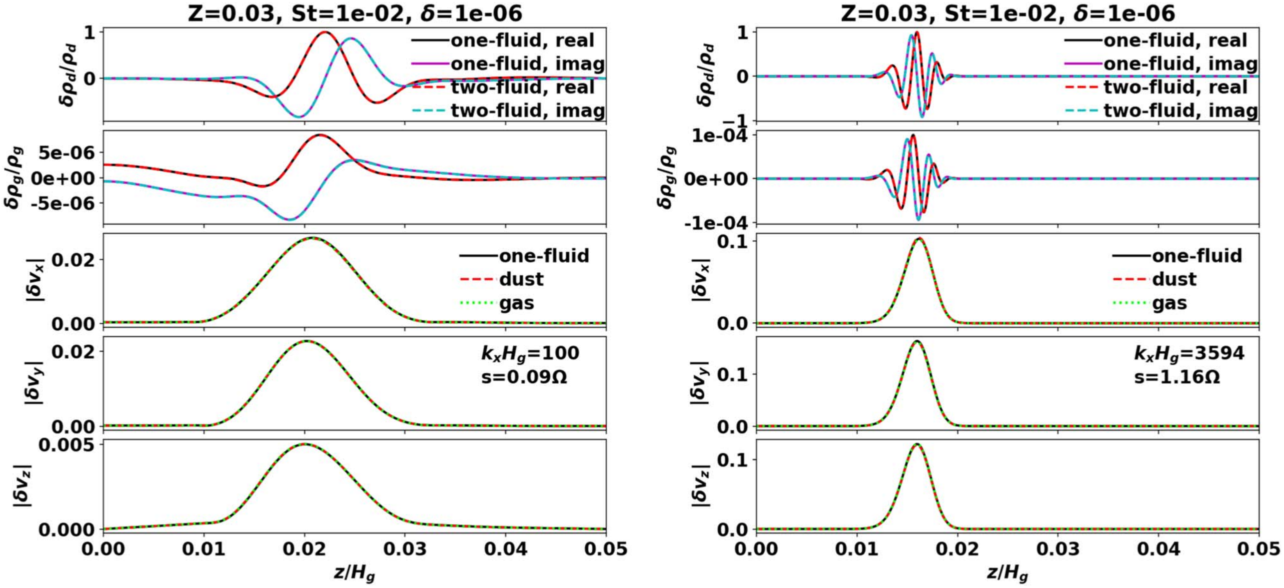

Figure 3. Normalized eigenfunctions of the most unstable modes found in case A (high dust density layer) with $K_x = 100$ (left) and $K_x \simeq 3594$ (right, also the most unstable over K_x). Perturbations from top to bottom: relative dust density, relative gas density, radial velocity, azimuthal velocity, and vertical velocity. For clarity, we plot the amplitudes of the velocity eigenfunctions.

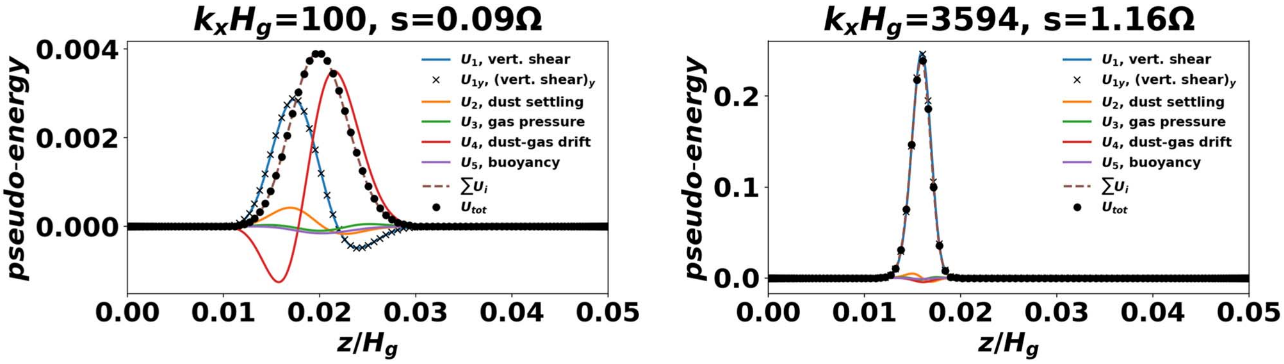

Figure 4. Pseudo-energy decomposition for the modes shown in Figure 3.

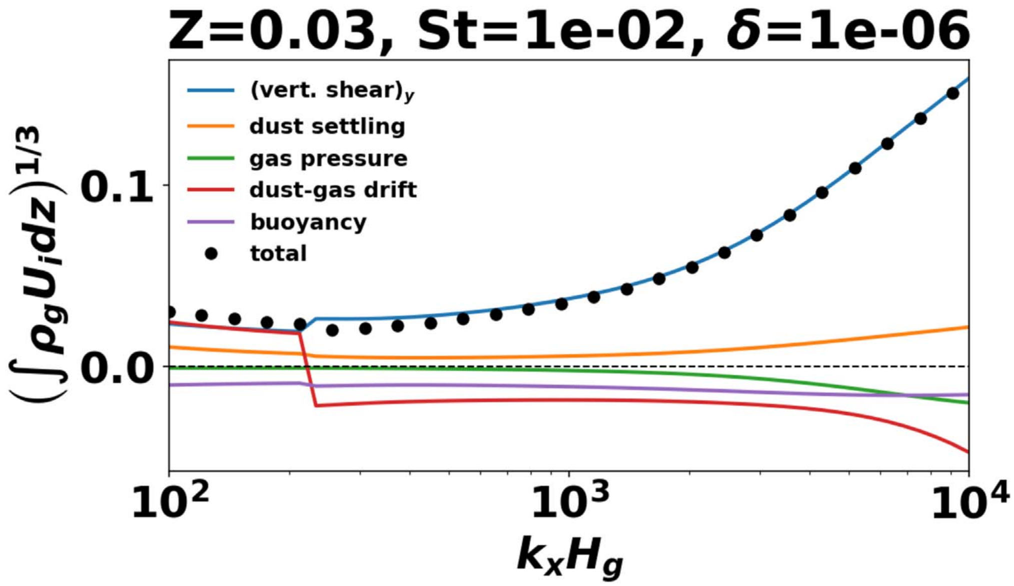

Figure 5. Vertically integrated pseudo-energy contributions for the most unstable modes in case A, as a function of K_x. Note that we plot the cube root for improved visualization.

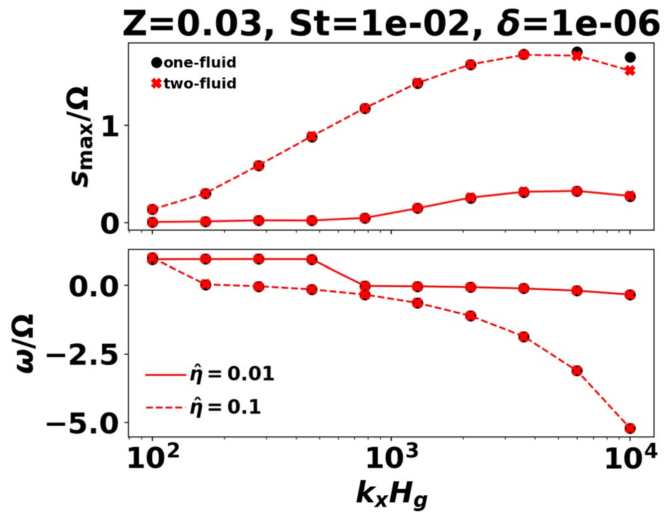

Figure 6. Maximum growth rate (top) and corresponding oscillation frequency (bottom) for unstable modes in case A (high dust density layer), with different values of the radial pressure gradient $\hat{\eta}=0.01$ (solid) and $\hat{\eta}=0.1$ (dashed).

5.1.2. Dependence on the Global Pressure Gradient

Figure 6 shows the effect the global radial pressure gradient, as measured by $\hat{\eta}\equiv \eta r/H_{\rm g}$. Note that dust–gas drift and vertical shear in the azimuthal velocity, which are the destabilizing effects for the modes we find, both scale with $\hat{\eta}$. This is consistent with the drift-driven classic SI, which also grows faster with increasing $\hat{\eta}$ at a fixed spatial scale (Jacquet et al. 2011; see their Equation (29)). For the vertical shear-driven unstable modes, the discussion in Section 6.1 also indicates that a minimum $\hat{\eta}$ is needed for instability (see Equation (58)). Hence, we find growth rates increase with $\hat{\eta}$.

We also find that the transition to modes purely driven by vertical shear occurs at smaller K_x for larger $\hat{\eta}$: $K_x > 100$ for $\hat{\eta}=0.1$ and $K_x > 500$ for $\hat{\eta}=0.01$. This is again similar to the gaseous VSI as a weaker vertical shear requires larger radial wavenumbers to destabilize (Latter & Papaloizou 2018).

5.1.3. Dependence on Particle Size

Here we consider Stokes numbers $\mathrm{St}=10^{-3}$ and $\mathrm{St}=0.1$.[6] The midplane dust-to-gas ratios are then ∼1 and ∼9, respectively (see Section 3.5.1). Growth rates and frequencies are shown in Figure 7. The trend for $\mathrm{St}=10^{-3}$ is qualitatively similar to our fiducial case with $\mathrm{St}=10^{-2}$, but with reduced growth rates. The modes again transition from drift-dominated to vertical shear-dominated as K_x increases, here beyond ∼400, somewhat higher than the fiducial case. The oscillation frequencies for the $\mathrm{St}=10^{-3}$ vertical shear modes are also much smaller in magnitude than that for $\mathrm{St}=10^{-2}$.

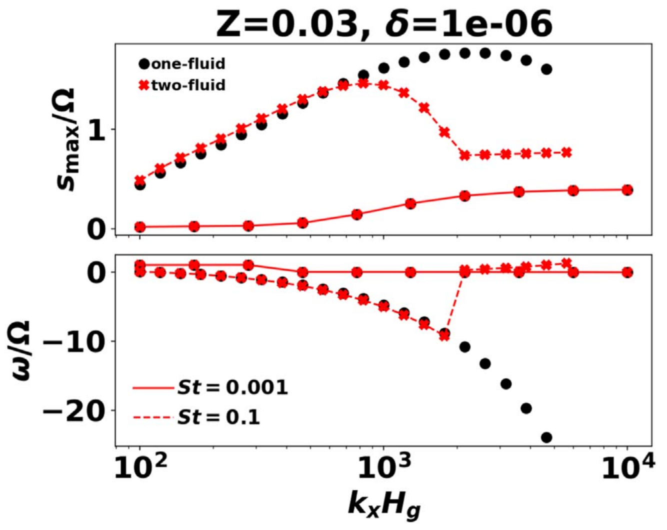

Figure 7. Maximum growth rate (top) and corresponding oscillation frequency (bottom) for unstable modes in case A (high dust density layer), with different Stokes numbers: $\mathrm{St}=10^{-3}$ (solid) and $\mathrm{St}=0.1$ (dashed).

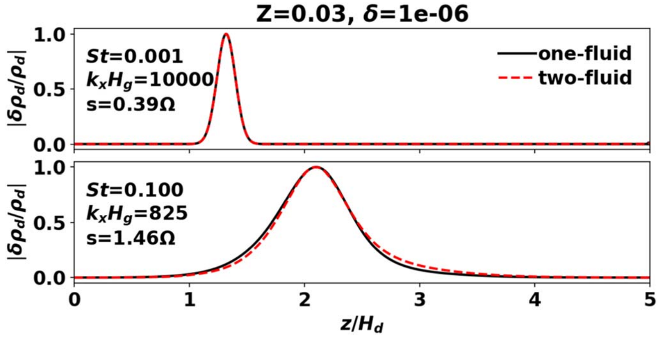

Figure 8. Magnitude of the relative dust density perturbation for the most unstable mode (over K_x, based on two-fluid growth rates) in case A with $\mathrm{St}=10^{-3}$ (top) and $\mathrm{St}=0.1$ (bottom).

For $\mathrm{St}=0.1$, the curves in Figure 7 are truncated at $K_x\gtrsim$ 5000–6000 as we were unable to find converged two-fluid solutions and one-fluid eigenfunctions were found to have large, unphysical oscillations near the disk boundary. Notice also the one-fluid model overpredicts growth rates for $K_x\gtrsim 10^3$. This is not surprising as the modes have $\mathrm{St}|\sigma|\gtrsim\Omega$, which can invalidate the one-fluid approximation (Lin & Youdin 2017; Paardekooper et al. 2020).

Nevertheless, we find that $\mathrm{St}=0.1$ growth rates exceed that for $\mathrm{St}=10^{-3}$. Moreover, all the $\mathrm{St}=0.1$ modes are driven by vertical shear. However, for $K_x\gtrsim 2000$, the two-fluid modes have nearly constant growth rates and were found to be centered around $z=3.3H_{\rm d}$, unlike the $K_x\lesssim 2000$ modes which are centered around $2H_{\rm d}$, including the most unstable mode.

The two-fluid results show that the most unstable modes in the $\mathrm{St}=10^{-3}$ and $\mathrm{St}=0.1$ disks occur at $K_x\gtrsim 10^4$ and $K_x\sim 825$, respectively. That is, instability with larger particles occur on larger radial scales. Figure 8 compares the vertical profiles in the relative dust density perturbations for the most unstable modes. Here, we rescale the vertical coordinate to account for different dust scale heights in these cases. For $\mathrm{St}=10^{-3}$, the mode is vertically localized with a characteristic length scale $l_z\simeq H_{\rm d}/2$, whereas for $\mathrm{St}=0.1$ we find $l_z\simeq 2H_{\rm d}$. Thus, instability with larger particles is also more global in the vertical direction.

We interpret the above results as looser dust–gas coupling provides more rapid "cooling" to mitigate buoyancy forces, which then allows destabilization of disturbances on longer length scales, similar to the gaseous VSI (Lin & Youdin 2015; see also Section 6.1).

---

[6] In the two-fluid calculation with $\mathrm{St}=0.1$, numerical artifacts developed near the disk surface, which were remedied by tapering the equilibrium vertical dust velocity to zero near the upper 10% of the domain. However, this had negligible effects on the growth rates, oscillation frequencies, or the eigenfunctions in the disk bulk.

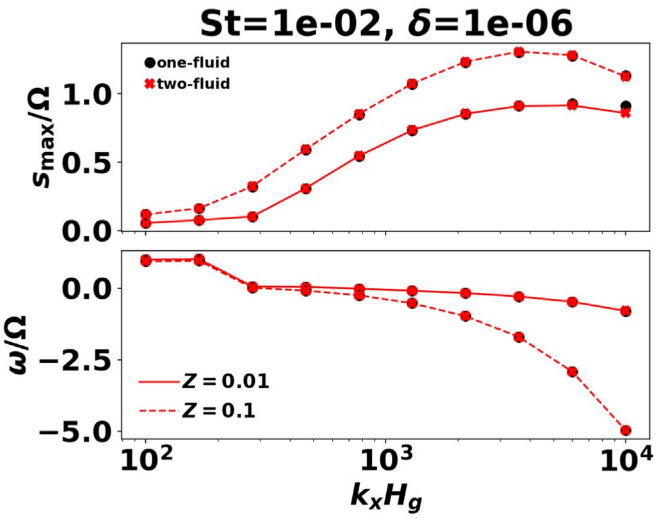

Figure 9. Maximum growth rate (top) and corresponding oscillation frequency (bottom) for unstable modes in case A (high dust density layer), with different metallicities: $Z = 0.01$ (solid) and $Z = 0.1$ (dashed).

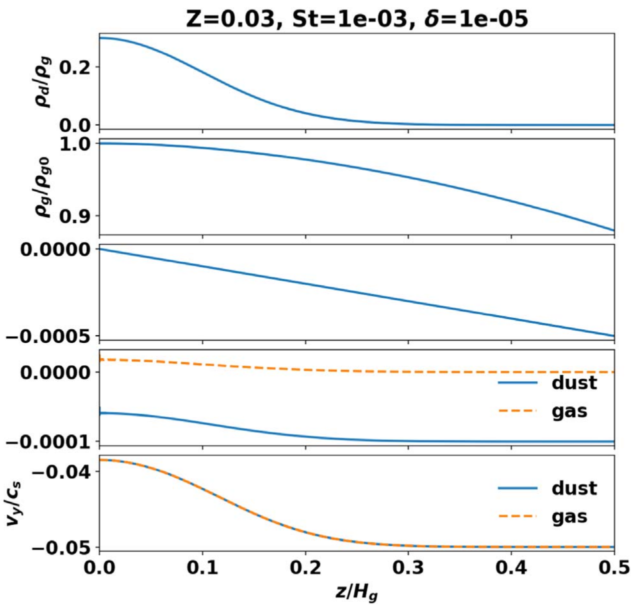

Figure 10. Two-fluid equilibrium for case B with a low dust density layer. From top to bottom: dust-to-gas ratio, gas density, vertical dust velocity, radial velocities, and azimuthal velocities.

5.1.4. Dependence on Dust Abundance

In Figure 9, we plot the maximum growth rates and corresponding frequencies for modes in disks with different metallicities. We find that growth rates modestly increase with increasing solid abundance, but overall the results are insensitive to Z. In particular, the transition from mixed modes to vertical shear-dominated modes does not depend on Z.

5.2. Case B: Low Dust Density Layer

We now consider a low dust density layer with $\epsilon < 1$ throughout the disk column by choosing a stronger diffusion coefficient, $\delta \simeq 10^{-5}$, and smaller particles, $\mathrm{St} = 10^{-3}$. Other parameters are the same as the fiducial setup in case A. The equilibrium disk profile for case B is shown in Figure 10.

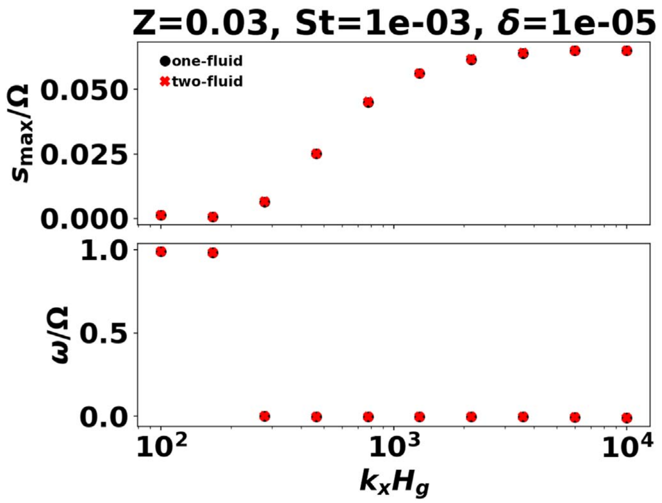

Figure 11. Maximum growth rate (top) and corresponding oscillation frequency (bottom) for unstable modes in case B (low dust density layer), as a function of the dimensionless radial wavenumber K_x.

Growth rates and oscillation frequencies for case B are shown in Figure 11. We again find two distinct classes of unstable modes: for $K_x < 200$, growth rates are small ($s \lesssim 10^{-2}\Omega$) with oscillation frequencies $O(\Omega)$, while for $K_x > 200$, modes are nearly purely growing with s saturating around 0.06Ω. Case B is much more stable than case A owing to the smaller dust-to-gas ratio and particle size.

Figure 12 shows the vertically integrated pseudo-energies. Modes with $K_x \lesssim 200$ are dominated by dust–gas drift with minor contributions from vertical shear and dust settling. This is unlike case A, where low-K_x modes have equal contributions from dust–gas drift and vertical shear. However, for $K_x \gtrsim 200$, modes are driven by vertical shear, as observed for case A.

Figure 13 shows that the mode with $K_x = 100$, primarily driven by dust–gas drift, involves ultra-short vertical oscillations of characteristic length scale $10^{-2}H_\mathrm{g}$, which is much smaller than $H_\mathrm{d} \simeq 0.1H_\mathrm{g}$. This should be compared to the case A mode in the left panel of Figure 3, which is driven by a combination of relative dust–gas radial drift and vertical shear and is more global, i.e., it varies on a scale comparable to the dust layer thickness. This suggests that vertical shear drives a more global disk response.

For the high-K_x modes driven mostly by vertical shear, we find similar behaviors in the eigenfunctions between case B and A: modes become increasingly localized with increasing K_x.

5.3. Case C: Viscous Disk

We briefly examine a viscous disk. To obtain appreciable growth rates in the presence of viscosity, we set $\alpha = 10^{-7}$. This value is much smaller than that expected in PPDs but is sufficient to demonstrate the impact of viscosity. We discuss this issue further in Section 6.3. Here, we use fiducial values of $\hat{\eta} = 0.05$ and $\mathrm{St} = 10^{-2}$, but set $Z = 0.01$ so that the midplane dust-to-gas ratio $\epsilon_0 \simeq 3$ is similar to case A. We also use a larger domain with $z_{\max} = 7H_\mathrm{d}$ as we find viscous modes at the smaller K_x values tend to be vertically extended, a result already hinted at by unstratified calculations (Chen & Lin 2020; Umurhan et al. 2020).

Figure 14 shows that the equilibrium structure for this viscous disk is qualitatively similar to case A (Figure 1), except

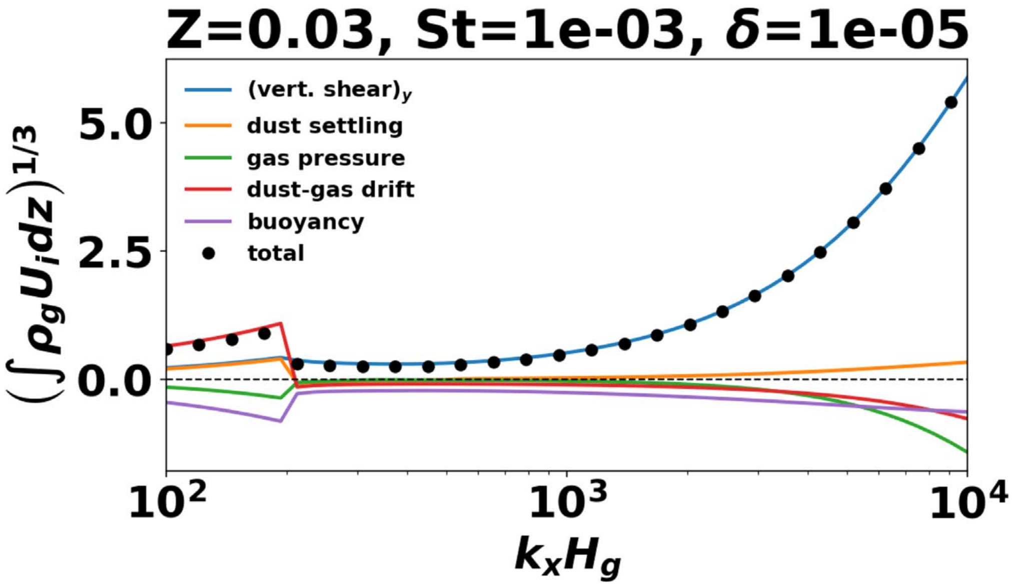

Figure 12. Vertically integrated pseudo-energy contributions for most unstable modes in case B as a function of K_x. Note that we plot the cube root for improved visualization.

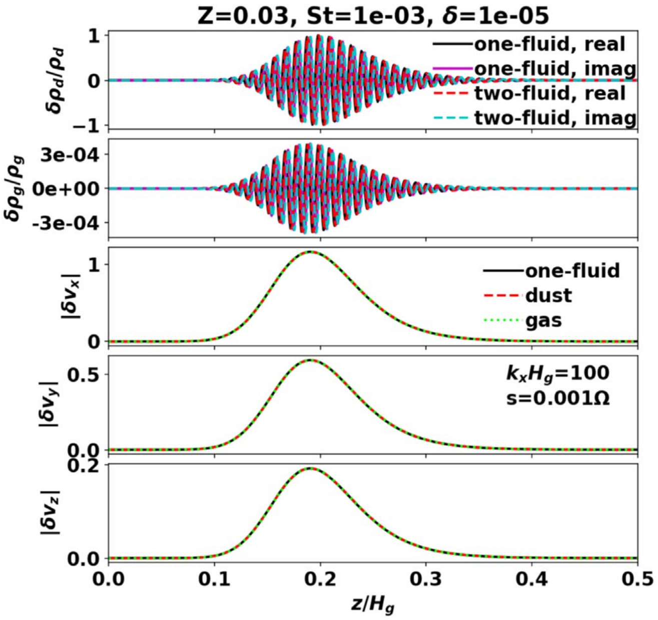

Figure 13. Normalized eigenfunctions of the most unstable mode found in case B (low dust density layer) with $K_x = 100$. Perturbations from top to bottom: relative dust density, relative gas density, radial velocity, azimuthal velocity, and vertical velocity. For clarity, we plot the amplitudes of the velocity eigenfunctions.

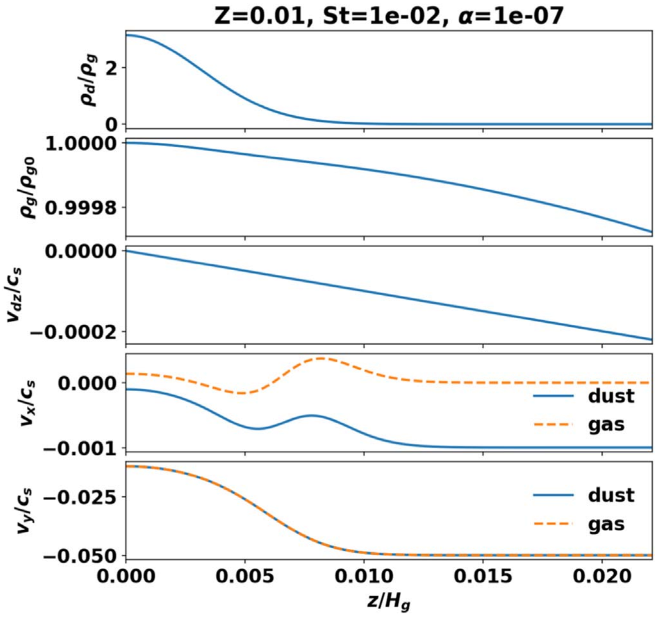

Figure 14. Two-fluid equilibrium for the viscous case C. From top to bottom: dust-to-gas ratio, gas density, vertical dust velocity, radial velocities, and azimuthal velocities.

in the radial velocities, which is noticeably nonmonotonic away from the midplane.

Figure 15 shows the growth rates of the most unstable modes as a function of K_x and corresponding oscillation frequencies. For comparison, we also plot results for an inviscid disk. We find viscosity strongly suppresses dust–gas instabilities. In the viscous disk, growth rates maximize at $K_x \simeq 1110$ with $s \sim 0.6\Omega$ and is essentially quenched for $K_x \gtrsim 4300$, while growth rates continue to increase with radial wavenumber in the inviscid disk.

In the left panel of Figure 16, we show a meridional visualization of the most unstable mode found for case C. The corresponding flow in the inviscid disk is shown in the right panel. As expected, viscosity tends produce vertically elongated disturbances, here with length scales ~1–2 H_{d}. This mode is again predominantly driven by vertical shear, as demonstrated by its pseudo-energy decomposition shown in Figure 17.

Figure 18 shows the vertically integrated pseudo-energy contributions to the unstable modes. Note that there is now a viscous contribution (brown curve); see Appendix C. For $K_x \lesssim 200$, unstable modes are driven by the relative dust–gas radial drift with minor contributions from dust settling. These modes have relatively small growth rates ($s \lesssim 0.1\Omega$). For $200 \lesssim K_x \lesssim 1300$, modes are driven by vertical shear with contributions from dust–gas drift. For $K_x \gtrsim 1300$, modes are

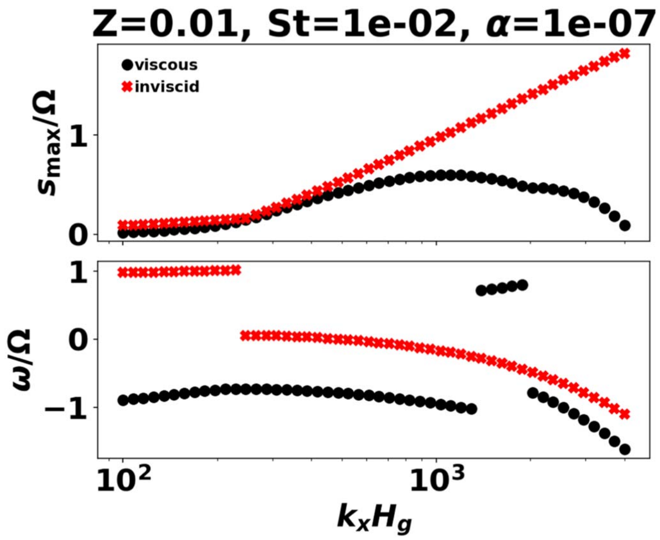

Figure 15. Growth rates (top) and oscillation frequencies (bottom) for modes found in the viscous case C (black circles) as a function of the dimensionless radial wavenumber K_x. Corresponding results for an inviscid disk are also shown (red crosses).

mostly driven by vertical shear, but their growth rates decline rapidly due to viscosity, which is more effective at stabilizing smaller length scales.

As expected, buoyancy and viscous forces always act to stabilize the system. On the other hand, dust settling is always destabilizing (Squire & Hopkins 2018b), although here its effect is small. Gas pressure has negligible effects, which reflects the incompressible nature of all unstable modes presented. Like inviscid cases A and B, we find that dust–gas drift becomes stabilizing at high radial wavenumbers (here $\gtrsim 10^3$). However, unlike those inviscid cases where vertical shear is always destabilizing, in the viscous disk we find that for low-K_x modes ($\lesssim 200$), vertical shear becomes stabilizing.

6. Discussion

6.1. Vertically Shearing Streaming Instabilities

Our numerical results show that the most unstable modes in stratified dust layers occur on radial length scales $\lesssim 10^{-3}H_g$ and are driven by the vertical gradient in the dusty disk's azimuthal velocity combined with partial dust−gas coupling. This is similar to the VSI in gaseous PPDs (Nelson et al. 2013). To interpret these VSSIs, we invoke the analogy between isothermal dusty gas and a pure gas subject to cooling as developed by Lin & Youdin (2017).

For the gaseous VSI, the destabilizing vertical shear results from the global radial temperature gradient. However, in PPDs, vertical gas buoyancy is strongly stabilizing. The gaseous VSI thus requires rapid cooling to remove the effect of buoyancy. In terms of these physical quantities, Lin & Youdin (2015) found the instability criterion

$$t_{\rm cool} < \frac{|\partial_z v_y|}{N_z^2}, \tag{52}$$

where $\partial_z v_y$ is the vertical shear rate, N_z is the vertical buoyancy frequency, and $t_{\rm cool}$ is the thermal cooling timescale such that the linearized cooling rate is

$$\delta\Lambda = -\frac{1}{t_{\rm cool}}\left(\delta P - \frac{P}{\rho_{\rm g}}\delta\rho_{\rm g}\right). \tag{53}$$

We can obtain a criterion analogous to Equation (52) for dusty disks as follows. We treat the isothermal dusty gas as a single fluid subject to a special cooling function, as described in Appendix B. The dusty disk's azimuthal velocity profile is given by Equation (B15). The vertical shear rate is thus

$$\frac{\partial v_y}{\partial z} = \frac{\eta r\Omega\epsilon'}{(1+\epsilon)^2}. \tag{54}$$

Next, Lin & Youdin (2017) showed that the square of the vertical buoyancy frequency in a dusty disk is

$$N_z^2 = c_{\rm s}^2\frac{\partial\ln\rho_{\rm g}}{\partial z}\frac{\partial f_{\rm d}}{\partial z},$$

where $f_{\rm d} = \epsilon/(1+\epsilon)$ is the dust fraction. Using the equilibrium condition (Equation (B8)), we find

$$N_z^2 = -\frac{z\Omega^2\epsilon'}{1+\epsilon}. \tag{55}$$

To estimate the appropriate "cooling time" in an isothermal dusty disk, we examine the one-fluid effective energy equation in Appendix B (Equation (B21)). We assume modes have small length scales and write $\partial_z \to ik_z$, where k_z is a real vertical wavenumber. Assuming both k_x and k_z are large in magnitude, the rhs of Equation (B21), which can be interpreted as a cooling rate after multiplying the equation by P, can be approximated by its leading term,

$$\delta\Lambda_{\rm d} \equiv -\frac{c_{\rm s}^2{\rm St}\epsilon k^2}{(1+\epsilon)^2\Omega}\delta P, \tag{56}$$

where $k^2 = k_x^2 + k_z^2$. Comparing Equation (56) with Equation (53) motivates the identification

$$t_{\rm cool,d} \equiv \frac{(1+\epsilon)^2\Omega}{c_{\rm s}^2{\rm St}\epsilon k^2} = \frac{(1+\epsilon)^2}{\epsilon{\rm St}K^2}\Omega^{-1} \tag{57}$$

as the cooling timescale of an isothermal dusty gas, where $K = kH_{\rm g}$.

Inserting Equations (57), (55), and (54) into Equation (52) gives the minimum wavenumber needed to trigger the dust-driven VSI,

$$K^2 > \frac{(1+\epsilon)^3}{\epsilon{\rm St}\hat{\eta}}\left(\frac{H_{\rm d}}{H_{\rm g}}\right)\frac{z}{H_{\rm d}}.$$

Note that the rhs is a function of height. To obtain a more practical criterion, we evaluate it at $z = H_{\rm d}$ and approximate $\epsilon \sim ZH_{\rm g}/H_{\rm d}$ (see Equation (3)). For settled dust layers with ${\rm St} \gg \delta$, as considered throughout this work, we have $H_{\rm d}/H_{\rm g} \simeq \sqrt{\delta/{\rm St}}$. These approximations then give

$$K^2 \gtrsim \frac{\left(1+Z\sqrt{{\rm St}/\delta}\right)^3\delta}{Z\hat{\eta}{\rm St}^2}. \tag{58}$$

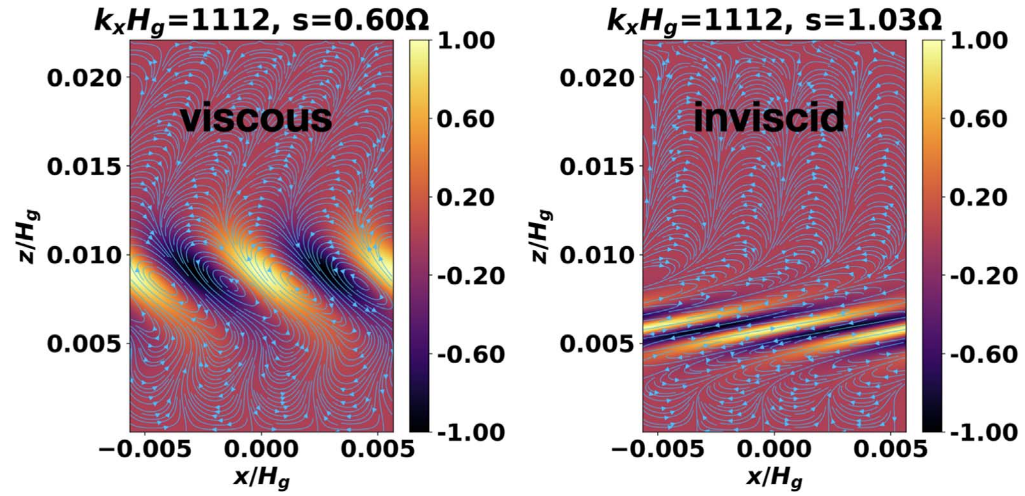

Figure 16. Structure of the most unstable mode found in the viscous case C (left, with $K_x \simeq 1110$) and the corresponding structure for an unstable mode in an inviscid disk with the same radial wavenumber. Streamlines correspond to the perturbed dust velocity field and colors correspond to the relative dust density perturbation.

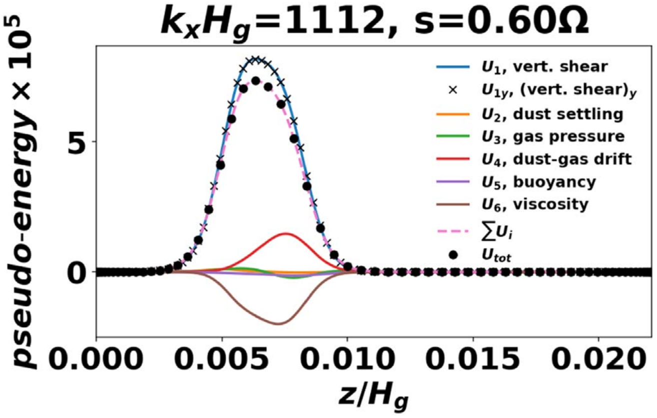

Figure 17. Pseudo-energy decomposition of the most unstable mode found in the viscous disk (case C).

Evaluating Equation (58) for the fiducial case A ($Z = 0.03$, $\mathrm{St} = 10^{-2}$, $\delta = 10^{-6}$, $\hat{\eta} = 0.05$) suggests $K \gtrsim 20$ is needed for finite dust−gas decoupling to destabilize the disk through vertical shear. Indeed, for case A, we find that the vertical shear contributes to the instability for all K_x considered ($\geqslant$100); see Figure 5.

On the other hand, for case B, we have $\mathrm{St} = 10^{-3}$ and $\delta \simeq 10^{-5}$, giving $K \gtrsim 120$. We thus expect that a much larger K_x is needed to tap into the free energy associated with vertical shear. Indeed, Figure 12 show that vertical shear is subdominant for modes below the transition at $K_x \sim 200$. This is similar to the gaseous VSI (Lin & Youdin 2015): a slower "cooling" rate, here associated with stronger dust−gas coupling, means it is can only effectively destabilize smaller length scales.

We remark that Equation (58) can also be applied to estimate the minimum radial pressure gradient needed to trigger VSSIs at a given spatial scale, which may explain the increasing growth rates with $\hat{\eta}$ seen in Section 5.1.2.

6.2. Comparison to Ishitsu et al. (2009)

Ishitsu et al. (2009) carried out direct simulations to investigate the effect of a vertical density gradient on the stability of dust layers. Their disk models were initialized with a prescribed, nonuniform vertical dust density distribution and corresponding horizontal velocity profiles given by Nakagawa et al. (1986). This is equivalent to stacking layers of unstratified disk models. They ignored vertical gravity, physical diffusion, viscosity, and assumed incompressible gas. We instead considered compressible gas (although this has negligible effects) and solve for the steady vertical disk structure self-consistently, which requires one to at least include dust diffusion.

Our results are broadly consistent with Ishitsu et al. Their simulation with $\mathrm{St} = 10^{-3}$ yields disturbances with characteristic wavenumber $k_x\eta r \sim 50$ (or $K_x \sim 10^3$ assuming $\hat{\eta} = 0.05$) and growth rate $\sim\Omega$. This is comparable to our case A with $\mathrm{St} = 10^{-3}$ in Section 5.1.3 (see Figure 7), for which we find growth rates of 0.2Ω–0.4Ω for $K_x \gtrsim 10^3$. Importantly, Ishitsu et al. also find that the vertical shear in the azimuthal velocity of the dust–gas mixture is the main driver of instability and that disturbances are centered off the disk midplane, similar to that observed in our VSSI eigenfunctions.

6.3. Gas Viscosity

The example in Section 5.3 (case C) showed that even a small amount of gas viscosity of $\alpha = 10^{-7}$ can reduce growth rates significantly. However, in PPDs, one may expect up to $\alpha \sim 10^{-4}$, for example, due to turbulence driven by the gaseous VSI (Manger et al. 2020). Here, we discuss two supplementary calculations to further explore the role of gas viscosity.

We first repeat the fiducial case A, but enable viscosity ($\alpha = 10^{-6}$) and use $z_{\max} = 7H_{\mathrm{d}}$. We find that the most unstable mode, shown in Figure 19, has $K_x \simeq 30$, $s \simeq 7 \times 10^{-4}\Omega$, and $\omega \simeq -3 \times 10^{-4}\Omega$, and is driven by vertical shear. Unsurprisingly, the mode has a much larger spatial scale than that for case C (see Figure 16), with a vertical length scale several times larger than H_{d} ($= 0.01H_{\mathrm{g}}$). However, the nonnegligible mode amplitudes near $z = z_{\max}$ indicate that boundary conditions may be important.

Next, we increase viscosity to $\alpha = 10^{-4}$, which alone would "puff up" the dust layer such that $\epsilon < 0.3$. We thus compensate by setting $Z = 0.3$ to obtain the same midplane dust-to-gas ratio as the above case ($\epsilon_0 \simeq 3$). We find that the most unstable

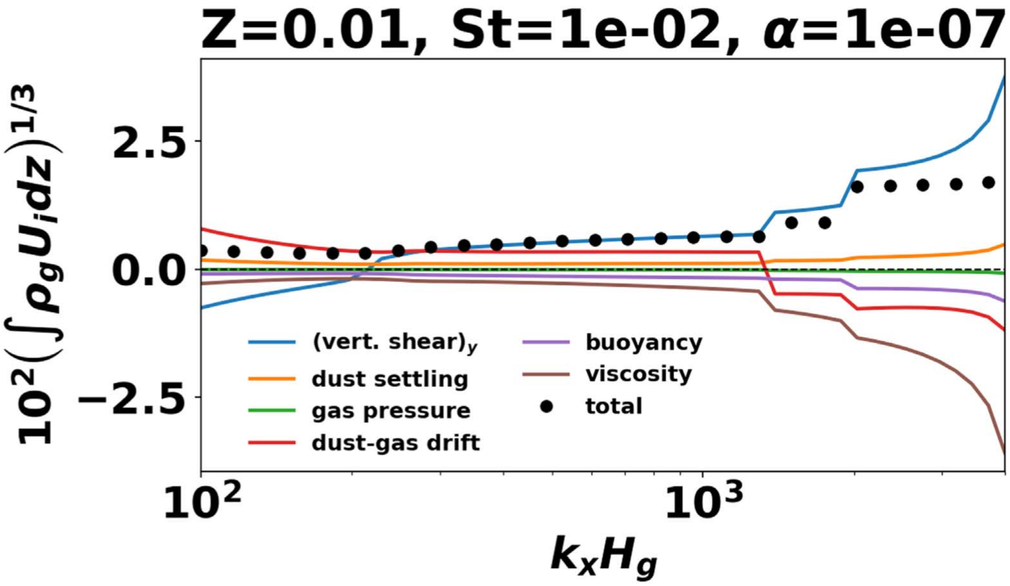

Figure 18. Vertically integrated pseudo-energy contributions to the most unstable modes found in the viscous case C, as a function of K_x. Note that we take the cube root for improved visualization.

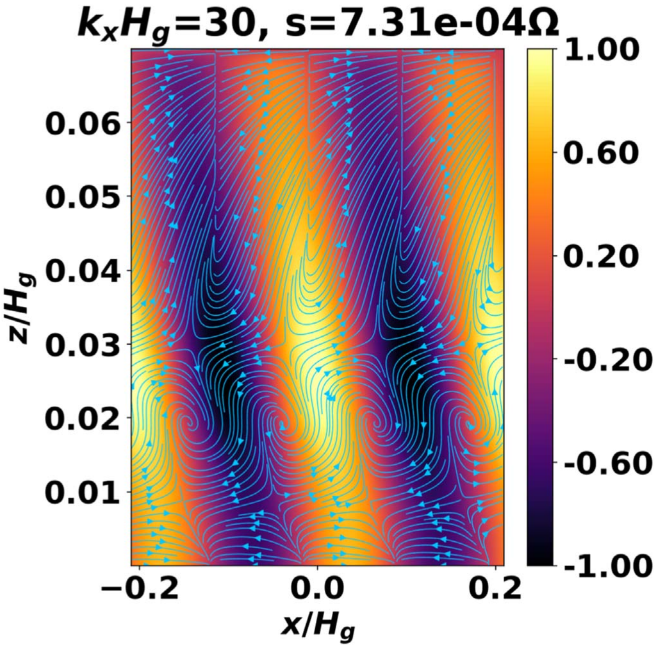

Figure 19. Structure of the most unstable mode in a viscous disk with $\alpha = 10^{-6}$ and other disk parameters taken from case A (see Section 5.1). Streamlines correspond to the perturbed dust velocity field and colors correspond to the relative dust density perturbation.

mode has $K_x \simeq 0.2$, $s \simeq 4 \times 10^{-4}\Omega$, and $s \simeq -\Omega$. Interestingly, the mode is found to have comparable contributions from vertical shear and dust settling. However, its radial length scale of order $\sim r$ (for $h_g = 0.05$) calls the shearing box framework itself into question.

Nevertheless, these calculations are instructive to show that viscosity is strongly stabilizing and produces disturbances that exceed the dust layer thickness, similar to the classic SI in unstratified, viscous disk models (Chen & Lin 2020; Umurhan et al. 2020).

6.4. Classic Streaming Instability

In unstratified disks, the classic SI of Youdin & Goodman (2005), driven by the dust–gas relative radial drift, is usually the only linearly unstable mode (but see Jaupart & Laibe 2020), which can lead to dust clumping in the nonlinear regime (Johansen & Youdin 2007).

In stratified disks, we find that the relative dust–gas drift can provide a significant (although not total) contribution to the most unstable modes on wavelengths of $O(10^{-2}H_g)$ or larger. Thus, we still refer to them as classic SI modes. If their nonlinear evolution is similar to their unstratified counterparts, then we can expect dust clumping on such scales.

However, classic SI modes are not the most unstable across all scales, which are the VSSI modes that occur on radial scales of $O(10^{-3}H_g)$ or smaller, as discussed above. The nonlinear evolution of classic SI modes will thus be affected by small-scale VSSIs that develop first. If VSSIs saturate in turbulence, as the early work of Ishitsu et al. appear to suggest (albeit based on simulations with a limited parameter range and integration times—see Section 6.7), then we expect a reduced efficiency of dust clumping via classic SIs.

In this case, we suggest that low-resolution (e.g., global) simulations that are biased toward classic SI modes should include a physical dust diffusion to mimic the effect of unresolved VSSI turbulence.

6.5. Dust-settling Instability

The DSI (Squire & Hopkins 2018b; Zhuravlev 2019, 2020) is an analog of the classic SI, except the DSI is driven by the vertical drift of dust relative to the gas (i.e., dust settling), rather than their relative radial drift. The DSI has been proposed to seed planetesimal formation by acting as a dust-clumping mechanism, although recent simulations show this effect may be weak in practice (Krapp et al. 2020). Studies of the DSI have so far adopted vertically local disk models, which ignore vertical shear but permit equilibria to be defined without dust diffusion. This is not possible in our vertically global disk models.

Our vertically global models confirm that dust settling acts to destabilize stratified dusty disks, which suggest that the DSI is present. However, it is generally subdominant to vertical shear, relative radial drift, or both. We can crudely understand this by comparing the dust-settling velocity $v_{\mathrm{d}z}$ to the azimuthal velocity difference across the dust layer, $H_{\mathrm{d}} v_y'$. Using Equations (19), (21), and (54), and considering $\mathrm{St} \ll 1$, we find

$$\left| \frac{H_{\mathrm{d}} v_y'}{v_{\mathrm{d}z}} \right| \simeq \frac{\epsilon}{(1+\epsilon)^2} \frac{\hat{\eta}}{\delta} \frac{H_{\mathrm{d}}}{H_{\mathrm{g}}} \sim \frac{Z\hat{\eta}}{(1+\epsilon)^2 \delta}, \tag{59}$$

where we used $Z \sim \epsilon H_{\mathrm{d}}/H_{\mathrm{g}}$ (see Equation (3)). We can further use $\delta \simeq \mathrm{St}Z^2/\epsilon^2$ to rewrite Equation (59) as $\sim\hat{\eta}/(\mathrm{St}Z)$, assuming $\epsilon \gtrsim 1$.

For the fiducial case A, we find Equation (59) gives ∼90, i.e., dust settling is dwarfed by vertical shear. Hence, for well-settled dust (small δ), instability is primarily due to vertical shear, provided its free energy can be accessed (see Section 6.1).

Dust settling may dominate over vertical shear if $\delta \gtrsim Z\hat{\eta}$. For PPDs with Z and $\hat{\eta}$ both of $O(10^{-2})$, this requirement translates to $\delta \gtrsim 10^{-4}$. However, such a large diffusion parameter is likely to be strongly stabilizing (Chen & Lin 2020; Krapp et al. 2020; Umurhan et al. 2020).

Similarly, we can compare settling to the dust–gas relative radial drift (Equation (1)), say at $z = H_{\mathrm{d}}$, to find

$$\left| \frac{v_{\mathrm{drift}}}{v_{\mathrm{d}z}} \right| \sim \frac{2\epsilon}{1+\epsilon} \frac{\hat{\eta}}{Z}, \tag{60}$$

again assuming $\mathrm{St} \ll 1$. In PPDs, the last factor is $O(1)$. Then, for settled dust layers with ϵ of $O(1)$, we expect settling to be at most comparable to radial drift. For well-mixed dust layers with $\epsilon \sim Z \sim O(10^{-2})$, the above ratio is $O(\hat{\eta}) \ll 1$ so that dust settling can dominate. However, having such an equilibrium requires a large diffusion coefficient ($\delta \gg \mathrm{St}$), which may provide complete stabilization.

6.6. Applicability of RDI Theory

Both the classic SI (for $\epsilon \ll 1$) and the DSI are RDIs (Squire & Hopkins 2018a, 2018b). RDIs arise when the background relative dust–gas motion resonates with a wave in the gas. The local condition for an RDI is

$$\boldsymbol{k} \cdot (\boldsymbol{v}_{\mathrm{d}} - \boldsymbol{v}_{\mathrm{g}}) = \omega_{\mathrm{gas}}(\boldsymbol{k}) \tag{61}$$

(Squire & Hopkins 2018a), where $\omega_{\mathrm{gas}}(\boldsymbol{k})$ is the frequency of a wave mode in the gas (when there is no dust) with local wavenumber $\boldsymbol{k}$. The small-ϵ classic SI and the DSI occur when radial dust drift and vertical dust settling resonate with inertial waves in the gas, respectively. It is then natural to ask whether or not vertically global modes in our stratified disks can be also interpreted as RDIs.

The first step of the RDI recipe given by Squire & Hopkins (2018b) is to choose a gas mode in the absence of dust. Fortunately, analytic dispersion relations can be obtained for stratified gas disks (Lubow & Pringle 1993; Lin & Youdin 2015). Specifically, inertial waves in an isothermal Keplerian disk satisfy

$$\omega_{\mathrm{gas}}^2 = \frac{L}{K_x^2 + L}\Omega^2, \tag{62}$$

where L is an integer, and it is assumed that $L \gg \omega_{\mathrm{gas}}^2/\Omega^2$ (Barker & Latter 2015; Lin & Youdin 2015).

Let us consider inertial waves with $L \gg K_x^2$. Then, $\omega_{\mathrm{gas}} \simeq \Omega$, as observed in the oscillation frequency for modes with $K_x = 100$ in cases A and B (see Figures 2 and 11, respectively). Using the radial drift and dust-settling velocities given by Equations (1) and (21), respectively, Equation (61) becomes

$$-2\hat{\eta}K_x - \frac{z}{H_{\mathrm{g}}}K_z = \frac{1}{\mathrm{St}},$$

where we have assumed $\mathrm{St}, \epsilon \ll 1$ and $K_z = k_z H_{\mathrm{g}}$. We can use this condition to estimate the vertical wavenumber K_z required for resonance.

Consider the $K_x = 100$ mode in case A with $\mathrm{St} = 10^{-2}$ and $z = 0.02H_{\mathrm{g}}$ or case B with $\mathrm{St} = 10^{-3}$ and $z = 0.2H_{\mathrm{g}}$, where radial drift and dust settling contribute to instability. The heights are chosen where mode amplitudes maximize; see Figures 3 (left panel) and 13. We then find $|K_z| \sim 5000$. However, the actual global eigenfunctions are better characterized by $|K_z| \sim 10^2$, indicating such modes do not reflect an RDI, at least locally. This discrepancy may be related to the fact that these modes are not purely associated with radial drift and dust settling: vertical shear also contributes (see Figures 5 and 12), but this effect does not enter local RDI theory.

On the other hand, the dominant VSSI modes are unrelated to the relative dust–gas motion in the background disk. Instead, it is associated with the single azimuthal velocity of the dust-plus-gas disk. It is thus unclear if VSSI modes can be interpreted as RDIs.

It will be necessary to develop a global RDI theory to address the above issues.

6.7. Implications for Planetesimal Formation

In nonlinear simulations, Ishitsu et al. (2009) showed that VSSI modes first lead to turbulence. They found large grains with unit St[7] then underwent clumping, possibly due to the classic SI, which is most effective for marginally coupled solids (Youdin & Goodman 2005). However, small grains ($\mathrm{St} = 10^{-3}$) were dispersed by the turbulence and did not clump, but this may be due to insufficient metallicities and integration times.

Recent simulations carried out by Yang et al. (2017) show that the clumping of small grains ($\mathrm{St} = 10^{-3}$–10^{-2}) require sufficient metallicities ($Z \gtrsim 0.02$–0.04) and integration times ($\gtrsim 10^2$–10^3 orbits). They also found dust clumping occurs after the disk saturates in a turbulent state. It is worth noting that the resolutions adopted in their simulations, of $O(10^{-4}H_{\mathrm{g}})$, should resolve VSSI modes, which we find to dominate on radial scales of $O(10^{-3}H_{\mathrm{g}})$.

Similarly, Bai & Stone (2010b) carried out three-dimensional simulations of stratified dusty disks, but found that the initial turbulence is largely axisymmetric, which rules out nonaxisymmetric KHIs as the cause (Chiang 2008; Lee et al. 2010). Given the large growth rates and axisymmetric nature of VSSIs, we suggest these were in fact responsible for the initial turbulence observed by Bai & Stone and Yang et al.

Similar to the gaseous VSI, VSSI turbulence is expected to erase the vertical shear responsible for it (Barker & Latter 2015), i.e., dust stratification, by vertically mixing up solids (Stoll & Kley 2016;

---

[7] This regime cannot be probed in our disk models because no equilibrium can be defined; see Section 3.5.1.

Flock et al. 2017; Lin 2019). Afterwards, we expect classic SI modes to become dominant. However, the ambient VSSI turbulence likely provides significant stabilization, especially for small grains (Chen & Lin 2020; Umurhan et al. 2020). This suggests that planetesimal formation in PPDs may be less efficient than estimates based on unstratified, laminar disk models, because VSSI turbulence should always be present in realistically stratified disks.

In light of the above discussion, we hypothesize the following interpretation of planetesimal formation as observed in previous simulations, e.g., Johansen et al. (2009). A thin, stratified dust layer first undergoes VSSIs. This leads to turbulence that renders the dust layer with almost uniform density and marginally stable against VSSIs, but still unstable to classic SI modes. The nonlinear evolution of the classic SI then produces dust clumps that, under appropriate conditions, leads to gravitational collapse into planetesimals.

6.8. Caveats and Outlooks

6.8.1. Analytical Models

We have relied on full numerical solutions to the linearized equations. Although our subsequent analyses hint at the physical origin of the various instabilities uncovered, a true understanding of the instability mechanisms require more rigorous mathematical modeling (Jacquet et al. 2011; Squire & Hopkins 2018b; Jaupart & Laibe 2020; Pan 2020; Pan & Yu 2020).

To this end, it is desirable to derive an algebraic dispersion relation for modes in a stratified dusty disk. This will allow us to classify modes and explain their growth as well as oscillation frequencies. This might be possible for the VSSI by exploiting the analogy between dust-laden flows and pure gas subject to cooling (Lin & Youdin 2017), as in the latter case analytic solutions for the gaseous VSI can be obtained (Lin & Youdin 2015).

6.8.2. Multiple Dust Species

We have only considered a single dust species. However, a distribution of particle sizes is expected in reality (Mathis et al. 1977; Birnstiel et al. 2012). Recent generalizations of the classic SI in unstratified disks show that having multiple dust species can significantly reduce growth rates when $\epsilon \lesssim 1$ (Krapp et al. 2019; Paardekooper et al. 2020; Zhu & Yang 2020). For the DSI, though, a particle size distribution has a limited effect (Krapp et al. 2020).

The VSSI is associated with the vertical shear of the dust-plus-gas system. Considering small, tightly coupled grains, all dust species and the gas share the same azimuthal velocity to O (St). We may thus naively expect the VSSI to be qualitatively similar for single and multiple dust species, if the two systems have the same dust-to-gas ratio profile and average Stokes number. This should be checked with explicit calculations.

One approach is to add vertical gravity and dust diffusion to the one-fluid model of a dusty gas with a continuous particle size distribution recently developed by Paardekooper et al. (2020). This is equivalent to adding one extra equation for the particle size-density to the one-fluid equations in Appendix B, which can then be implemented in the codes developed for this study.

6.8.3. Dust Diffusion Model

We adopted a simple dust diffusion model so that stratified equilibria can be defined and standard linear stability analyses can be carried out. Physically, this model assumes there exists an underlying, external mechanism that stirs up dust grains, such as turbulence. In our implementation, this is characterized by a single, constant diffusion coefficient. However, realistic turbulence may depend on the disk structure. For example, turbulence driven by the gaseous VSI can be reduced by dust loading (Lin 2019; Schäfer et al. 2020). In this case, particle diffusion within the dusty midplane should be weaker than the dust-free gas above and below it.

Particle stirring may also result from dust–gas instabilities itself. Consider, for example, an initially laminar disk. As grains settle, it may (instantaneously) meet the conditions for the classic SI, dust-driven VSI, KHIs, or others. However, to properly describe how a settling dust layer becomes unstable, one needs to perform stability analyses with respect to nonsteady backgrounds (e.g., Garaud & Lin 2004), which is beyond the scope of this work. Nevertheless, such instabilities are thought to drive turbulence that prevents further settling (e.g., Johansen et al. 2009) and maintain a quasi-steady state.

In the above contexts, our study should be interpreted as the stability of dust layers whose equilibrium state is maintained by turbulence driven by preexisting dust–gas instabilities. To better reflect realistic PPDs, our models should thus be generalized to diffusion (and possibly gas viscosity) coefficients with strength and spatial dependencies based on explicit simulations of quasi-steady, turbulent dust layers (e.g., Bai & Stone 2010b; Yang et al. 2017).

A more fundamental issue with the adopted diffusion model, though common, is that it can lead to nonconservation of total angular momentum (Tominaga et al. 2019). However, we suspect this will not qualitatively affect the VSSI as it is unrelated to dust diffusion: Ishitsu et al. observed the same instabilities, but only included a small diffusion term for numerical stability. Nevertheless, it would be useful to examine the VSSI in the angular-momentum-conserving formalism developed by Tominaga et al.

6.8.4. Nonaxisymmetry

Finally, we considered axisymmetric perturbations exclusively, which preclude nonaxisymmetric KHIs (Chiang 2008; Lee et al. 2010). The growth of KHIs and the axisymmetric instabilities presented in this work should be compared to assess which is more relevant in PPDs. However, in the shearing box framework, linear, nonaxisymmetric disturbances may only undergo transient or algebraic growth (e.g., Balbus & Hawley 1992; Johnson & Gammie 2005). Describing them requires one to solve an initial value problem, rather than the eigenvalue problem herein. Alternatively, one can forgo the plane wave ansatz and compute the full radial structure of linear disturbances with nonperiodic boundary conditions (e.g., Adams et al. 1989; Savonije & Heemskerk 1990; Lin & Papaloizou 2011a, 2011b). However, this would result in a partial differential equation eigenvalue problem (e.g., Lin 2013), which is significantly more complex than that considered in this work .

7. Summary

In this paper, we study the axisymmetric linear stability of vertically stratified dust layers in PPDs. Our disk models extend those used to study the classic SI (Youdin & Goodman 2005), namely unstratified disks, by accounting for the vertical structure of dust and gas in PPDs, as small solids are expected to settle near the disk midplane.

We find that the dominant instability in stratified disks is one driven by the vertical gradient in the dusty gas' azimuthal velocity. The large vertical shear within a settled dust layer is a significant source of free energy, which can be accessed via partial dust–gas coupling. This allows unstable modes to grow on orbital timescales. Our findings are consistent with earlier nonlinear simulations carried out by Ishitsu et al. (2009).

In PPDs, these VSSIs occur on radial scales $\lesssim 10^{-3}H_{\rm g}$, where $H_{\rm g}$ is the local gas scale height. On the other hand, classic SI modes, associated with the relative radial drift between dust and gas, occur on radial length scales $\gtrsim 10^{-2}H_{\rm g}$, but have much smaller growth rates than VSSIs.

However, the nonlinear evolution of VSSIs may drive turbulence that mixes up the dust layer (Ishitsu et al. 2009), rather than dust clumping like the classic SI (Johansen & Youdin 2007). Given their dynamical growth rates, we suggest VSSI turbulence may have already manifested in some simulations (e.g., Bai & Stone 2010b; Yang et al. 2017), which show that stratified dust layers first settle into a quasi-steady, turbulent state before clumping.

If VSSIs are inherent to PPDs and its primary outcome is turbulence, then planetesimal formation through the classic SI may be less efficient than previously thought, as clumping will always be hindered by small-scale VSSI turbulence. High-resolution simulations that fully resolve VSSI scales will be necessary to clarify this issue.

I thank the anonymous referee for a thorough report that considerably improved the connection between this work and the literature. I thank Volker Elling, Pin-Gao Gu, Ming-Chih Lai, Yueh-Ning Lee, Te-Sheng Lin, Jack Ng, Debanjan Sengupta, Ryosuke Tominaga, Orkan Umurhan, and David C.C. Yen for useful discussions, tips, and advice. This work is supported by Taiwan's Ministry of Science and Education through grant 107-2112-M001-043-MY3.

Appendix A
List of Symbols

Table 2 summarizes the frequently used and related symbols in the main text.

Table 2
Frequently Used Symbols

Notation	Definition	Description
$\rho_{\rm d,g}$		Dust and gas densities
$\boldsymbol{v}_{\rm d,g}$		Dust and gas velocities in the shearing box, relative to Keplerian flow
ϵ, ϵ_0	$\rho_{\rm d}/\rho_{\rm g}$, $\epsilon(z=0)$	Local dust-to-gas ratio, midplane dust-to-gas ratio
$\Sigma_{\rm d,g}$	$\int_{-\infty}^{\infty}\rho_{\rm d,g}dz$	Dust and gas surface densities
Z	$\Sigma_{\rm d}/\Sigma_{\rm g}$	Metallicity
$c_{\rm s}$		Constant gas sound speed
Ω	$\sqrt{GM_*/r^3}$	Keplerian rotation frequency
$H_{\rm g}$, $h_{\rm g}$	$c_{\rm s}/\Omega$, $H_{\rm g}/r$	Gas disk pressure scale height, aspect ratio
P	$c_{\rm s}^2\rho_{\rm g}$	Pressure in the global disk or local pressure fluctuations in the shearing box
η, $\hat{\eta}$	$-(2r\Omega^2\rho_{\rm g})^{-1}\partial_r P$, $\eta/h_{\rm g}$	Dimensionless global pressure gradient, reduced pressure-gradient parameter
α		Dimensionless gas viscosity
δ	$(1+{\rm St}+4{\rm St}^2)/(1+{\rm St}^2)^2\alpha$	Dimensionless dust diffusion coefficient
St	$\tau_{\rm s}\Omega$	Stokes number with particle stopping time $\tau_{\rm s}$
$H_{\rm d}$	$\sqrt{\delta/(\delta+{\rm St})}H_{\rm g}$	Dust scale height
$\delta\rho_{\rm g}$, etc.		Complex amplitude of Eulerian perturbations (eigenfunctions)
s, ω	${\rm Re}(\sigma)$, $-{\rm Im}(\sigma)$	Growth rate, oscillation frequency of the complex growth rate σ
K_x	$k_xH_{\rm g}$	Dimensionless radial wavenumber

Appendix B
One-fluid Model of Dusty Gas in the Shearing Box

In the "one-fluid" description of dusty gas, we work with the total density

$$\rho = \rho_{\mathrm{g}} + \rho_{\mathrm{d}} \tag{B1}$$

and center-of-mass velocity

$$\boldsymbol{v}_c = \frac{\rho_{\mathrm{g}}\boldsymbol{v}_{\mathrm{g}} + \rho_{\mathrm{d}}\boldsymbol{v}_{\mathrm{d}}}{\rho}. \tag{B2}$$

Furthermore, by considering small, tightly coupled dust particles we relate the gas and dust velocities by the "terminal velocity approximation,"

$$\boldsymbol{v}_{\mathrm{d}} = \boldsymbol{v}_{\mathrm{g}} + t_{\mathrm{s}}\left(\frac{\nabla P}{\rho_{\mathrm{g}}} - 2\eta r\Omega^2\hat{\boldsymbol{x}}\right) \tag{B3}$$

(Youdin & Goodman 2005; Laibe & Price 2014). Here, $t_{\mathrm{s}} = \tau_{\mathrm{s}}\rho_{\mathrm{g}}/\rho$ is the relative stopping time. Recall that $\boldsymbol{v}_{\mathrm{d,g}}$ are dust and gas velocities in the shearing box relative to the Keplerian flow, respectively, and P is the local pressure fluctuation. The term $\propto \eta$ represents the radial pressure gradient in the global disk. Thus, in the unperturbed state with vanishing P, dust drifts radially relative to the gas.

The dust–gas mixture is modeled as a single, adiabatic fluid with a special cooling function (Lin & Youdin 2017; Lovascio & Paardekooper 2019). Dropping the subscript "c" for clarity, our one-fluid model equations in the local shearing box to $O(t_{\mathrm{s}})$ are

$$\frac{\partial \rho}{\partial t} + \nabla\cdot(\rho\boldsymbol{v}) = \nabla\cdot(D\rho_{\mathrm{g}}\nabla\epsilon), \tag{B4}$$

$$\frac{\partial \boldsymbol{v}}{\partial t} + \boldsymbol{v}\cdot\nabla\boldsymbol{v} = -\frac{\nabla P}{\rho} + 2\eta r\Omega^2\frac{\rho_{\mathrm{g}}}{\rho}\hat{\boldsymbol{x}} + 2\Omega v_y\hat{\boldsymbol{x}} - \frac{\Omega}{2}v_x\hat{\boldsymbol{y}} - \Omega^2 z\hat{\boldsymbol{z}}, \tag{B5}$$

$$\frac{\partial P}{\partial t} + \nabla\cdot(P\boldsymbol{v}) = c_{\mathrm{s}}^2\nabla\cdot[t_{\mathrm{s}}f_{\mathrm{d}}(\nabla P - 2\eta r\Omega^2\rho_{\mathrm{g}}\hat{\boldsymbol{x}})]. \tag{B6}$$

(Laibe & Price 2014; Lin & Youdin 2017; Lovascio & Paardekooper 2019; Chen & Lin 2020; Paardekooper et al. 2020), where $f_{\mathrm{d}} \equiv \rho_{\mathrm{d}}/\rho$ is the dust fraction. Note that $\rho_{\mathrm{g}} = P/c_{\mathrm{s}}^2$ for the isothermal gas we consider, so $f_{\mathrm{d}} = 1 - P/c_{\mathrm{s}}^2\rho$. The second term on the rhs of Equation (B5) vanishes in a particle disk where $\rho_{\mathrm{g}} \to 0$, because solids do not feel pressure gradients. Conversely, for a dust-free gas disk ($\rho_{\mathrm{g}}/\rho \to 1$), we recover the full pressure support from the global disk. The second term in the parentheses on the rhs of Equation (B6) arises from the contribution to the terminal velocity approximation from the large-scale radial pressure gradient in Equation (B3).

B.1. Approximate Equilibria

As in the two-fluid model, we seek steady, horizontally uniform solutions. The mass, energy, and vertical momentum equations are then

$$\rho v_z = D\rho_{\mathrm{d}}(\ln\epsilon)', \tag{B7}$$

$$v_z v_z' = -\frac{P'}{\rho} - \Omega^2 z \simeq 0, \tag{B8}$$

$$P v_z = c_{\mathrm{s}}^2 t_{\mathrm{s}} f_{\mathrm{d}} P', \tag{B9}$$

where in Equation (B8) we ignore the $O(v_z^2)$ term a posteriori for consistency with the small t_{s} approximation used to derive the one-fluid model. These equations may then be solved for constant $\tau_{\mathrm{s}} = t_{\mathrm{s}}/f_g = \mathrm{St}/\Omega$ to yield

$$\epsilon = \epsilon_0 \exp\left(-\frac{\mathrm{St}}{2\delta}\frac{z^2}{H_{\mathrm{g}}^2}\right), \tag{B10}$$

$$v_z = -\frac{\epsilon}{1+\epsilon}\mathrm{St}z\Omega, \tag{B11}$$

$$P = P_0 \exp\left[\frac{\delta}{\mathrm{St}}(\epsilon - \epsilon_0) - \frac{z^2}{2H_{\mathrm{g}}^2}\right]. \tag{B12}$$

From here, it is clear that $v_z = O(\mathrm{St})$, so it is self-consistent to ignore the $O(v_z^2)$ term. Equations (B10)–(B12) are in fact the same solutions as in the full two-fluid model in the limit $\mathrm{St} \ll 1$ (see Equations (19)–(21); recall $\beta \to \mathrm{St}$ for $\mathrm{St} \to 0$ and note $v_z = f_{\mathrm{d}}v_{\mathrm{d}z}$).

The horizontal momentum equations are

$$v_z v_x' = 2\eta r\Omega^2\frac{\rho_{\mathrm{g}}}{\rho} + 2\Omega v_y \simeq 0, \tag{B13}$$

$$v_z v_y' = -\frac{\Omega}{2}v_x, \tag{B14}$$

where we ignore the quadratic term in Equation (B13) to obtain

$$v_y = -\frac{\eta r\Omega}{1+\epsilon}. \tag{B15}$$

This is expected on physical grounds for tightly coupled dust ($\mathrm{St} \to 0$). In this limit, the mixture behaves close to a single fluid with orbital velocity depending on the level of dust enrichment. For $\epsilon \to 0$, we have a pressure-supported gas disk at sub-Keplerian velocity (assuming $\eta > 0$), while $\epsilon \to \infty$ corresponds to a particle disk on exactly Keplerian orbits, because then $v_y \to 0$.

Next, we use Equations (B15), (B14), and (B11) to obtain

$$v_x = -\frac{2}{\Omega}v_z v_y' = \frac{2\eta r\Omega\epsilon\epsilon'}{(1+\epsilon)^3}\mathrm{St}z. \tag{B16}$$

Notice the radial velocity of the dust–gas mixture's center of mass depends on height. It is only zero at the midplane and for $|z| \to \infty$ where $\epsilon \to 0$. For $\eta > 0$, the specific angular momentum decreases with increasing $|z|$: the mixture gains pressure support as it becomes more gas-rich away from the midplane. This means that as a parcel of the mixture settles, it finds itself having an angular-momentum deficit compared to its surrounding; it thus drifts inwards ($v_x < 0$), as indicated by Equation (B16).

B.2. Linearized Equations

We linearize the one-fluid equations about the above basic state, with nonuniform $v_x(z)$, $v_y(z)$, and $v_z(z)$. As in the main text, we assume axisymmetric perturbations in the form of $\delta\rho(z)\exp(\sigma t + ik_x x)$ and similarly for other variables. The linearized equations are

$$\begin{aligned}&\sigma\frac{\delta\rho}{\rho}+ik_x\left(\delta v_x+v_x\frac{\delta\rho}{\rho}\right)+\frac{\rho'}{\rho}\left(v_z\frac{\delta\rho}{\rho}+\delta v_z\right)\\&\quad+v_z\left(\frac{\delta\rho}{\rho}\right)'+v_z'\frac{\delta\rho}{\rho}+\delta v_z'\\&\quad=Df_{\mathrm{d}}\left[Q''-k_x^2Q+\frac{\rho_{\mathrm{d}}'}{\rho_{\mathrm{d}}}\left(\frac{\epsilon'}{\epsilon}\frac{\delta\rho_{\mathrm{d}}}{\rho_{\mathrm{d}}}+Q'\right)\right.\\&\quad\left.+\frac{\epsilon'}{\epsilon}\left(\frac{\delta\rho_{\mathrm{d}}}{\rho_{\mathrm{d}}}\right)'+(\ln\epsilon)''\frac{\delta\rho_{\mathrm{d}}}{\rho_{\mathrm{d}}}\right],\end{aligned}\tag{B17}$$

$$\begin{aligned}&\sigma\delta v_x+ik_xv_x\delta v_x+v_x'\delta v_z+v_z\delta v_x'\\&\quad=-ik_x\frac{P}{\rho}W-\frac{2\eta r\Omega^2\epsilon}{(1+\epsilon)^2}Q+2\Omega\delta v_y,\end{aligned}\tag{B18}$$

$$\sigma\delta v_y+ik_xv_x\delta v_y+v_y'\delta v_z+v_z\delta v_y'=-\frac{\Omega}{2}\delta v_x,\tag{B19}$$

$$\sigma\delta v_z+ik_xv_x\delta v_z+v_z'\delta v_z+v_z\delta v_z'=\frac{P'}{\rho}\frac{\epsilon Q}{1+\epsilon}-\frac{P}{\rho}W',\tag{B20}$$

$$\begin{aligned}&\sigma W+ik_x(\delta v_x+v_xW)+\frac{P'}{P}(v_zW+\delta v_z)\\&\quad+v_z'W+v_zW'+\delta v_z'\\&\quad=\frac{\mathcal{K}}{P}\left[W''-k_x^2W+\frac{\mathcal{K}'}{\mathcal{K}}\left(\frac{P'}{P}\frac{\delta\mathcal{K}}{\mathcal{K}}+W'\right)\right.\\&\quad\left.+\frac{P'}{P}\left(\frac{\delta\mathcal{K}}{\mathcal{K}}\right)'+(\ln P)''\frac{\delta\mathcal{K}}{\mathcal{K}}\right]\\&\quad-2ik_x\eta r\Omega^2\frac{\mathcal{K}}{c_s^2P}\left[\left(\frac{1-\epsilon}{1+\epsilon}\right)Q+W\right],\end{aligned}\tag{B21}$$

where

$$\mathcal{K}\equiv\frac{c_s^2P\mathrm{St}\epsilon}{\Omega(1+\epsilon)^2},\tag{B22}$$

and recall $Q=\delta\epsilon/\epsilon$ and $W=\delta\rho_{\mathrm{g}}/\rho_{\mathrm{g}}=\delta P/P$.

B.3. Mode Energetics

Following Ishitsu et al. (2009), we multiply the x, y, and z momentum equations (Equations (B18)–(B20)) by $\delta v^*_{x,y,z}$, respectively, combine them appropriately, then take the real part. We also scale the overall result by a factor of $(1+\epsilon)$ for easier comparison with the corresponding two-fluid treatment in Appendix C. The one-fluid result is

$$E_{\mathrm{tot}}\equiv(1+\epsilon)(|\delta v_x|^2+4|\delta v_y|^2+|\delta v_z|^2)=\sum_{i=1}^{5}E_i,\tag{B23}$$

with

$$\begin{aligned}sE_1=&-(1+\epsilon)[v_x'\,\mathrm{Re}\,(\delta v_z\delta v_x^*)\\&+4v_y'\,\mathrm{Re}\,(\delta v_z\delta v_y^*)+v_z'\,|\delta v_z|^2]\\\equiv&\ sE_{1x}+sE_{1y}+sE_{1z}\end{aligned}\tag{B24}$$

$$sE_2=-v_z(1+\epsilon)\mathrm{Re}\,(\delta v_x'\delta v_x^*+4\delta v_y'\delta v_y^*+\delta v_z'\delta v_z^*)\tag{B25}$$

$$sE_3=c_s^2[k_x\,\mathrm{Im}\,(W\delta v_x^*)-\mathrm{Re}\,(W'\delta v_z^*)]\tag{B26}$$

$$sE_4=-\frac{2\eta r\Omega^2\epsilon}{(1+\epsilon)}\mathrm{Re}\,(Q\delta v_x^*)=\frac{\epsilon\Omega(v_{\mathrm{d}x}-v_{\mathrm{g}x})}{\mathrm{St}}\mathrm{Re}\,(Q\delta v_x^*)\tag{B27}$$

$$\begin{aligned}sE_5=&-\epsilon z\Omega^2\,\mathrm{Re}\,(Q\delta v_z^*)\\=&-z\Omega^2(1+\epsilon)\mathrm{Re}\left[\left(\frac{\delta\rho}{\rho}-\frac{\delta P}{P}\right)\delta v_z^*\right].\end{aligned}\tag{B28}$$

The factor of 4 in the expression for E_{tot} is introduced to eliminate the rotation terms in Equations (B18) and (B19). E_1 is associated with the vertical shear in the equilibrium velocities, E_2 is associated with dust settling, and E_3 is associated with pressure forces. In the second equality for E_4, we used Equation (B3) to relate the global radial pressure gradient to the dust–gas radial drift in steady state. For E_5, we used the equilibrium condition $P'/\rho\simeq-z\Omega^2$ and in the second equality used the fact that the total density $\rho\propto P(1+\epsilon)$ to relate the perturbed dust-to-gas ratio to pressure and density perturbations. From this, it is clear that E_5 is associated with buoyancy effects, i.e., pressure–density perturbation mismatches.

Appendix C
Two-fluid Pseudo-energy Decomposition

Following the same procedure as in the one-fluid treatment (Appendix B.3), we can define the pseudo-energy in the full two-fluid framework as

$$\begin{aligned}U_{\mathrm{tot}}=&\ \epsilon(|\delta v_{\mathrm{d}x}|^2+4|\delta v_{\mathrm{d}y}|^2+|\delta v_{\mathrm{d}z}|^2)\\&+|\delta v_{\mathrm{g}x}|^2+4|\delta v_{\mathrm{g}y}|^2+|\delta v_{\mathrm{g}z}|^2=\sum_{i=1}^{6}U_i,\end{aligned}\tag{C1}$$

with

$$\begin{aligned}sU_1=&-[\epsilon v_{\mathrm{d}x}'\,\mathrm{Re}\,(\delta v_{\mathrm{d}z}\delta v_{\mathrm{d}x}^*)+v_{\mathrm{g}x}'\,\mathrm{Re}\,(\delta v_{\mathrm{g}z}\delta v_{\mathrm{g}x}^*)]\\&-4[\epsilon v_{\mathrm{d}y}'\,\mathrm{Re}\,(\delta v_{\mathrm{d}z}\delta v_{\mathrm{d}y}^*)+v_{\mathrm{g}y}'\,\mathrm{Re}\,(\delta v_{\mathrm{g}z}\delta v_{\mathrm{g}y}^*)]\\&-\epsilon v_{\mathrm{d}z}'\,|\delta v_{\mathrm{d}z}|^2,\\\equiv&\ sU_{1x}+sU_{1y}+sU_{1z},\end{aligned}\tag{C2}$$

$$sU_2=-\epsilon v_{\mathrm{d}z}\,\mathrm{Re}\,(\delta v_{\mathrm{d}x}'\delta v_{\mathrm{d}x}^*+4\delta v_{\mathrm{d}y}'\delta v_{\mathrm{d}y}^*+\delta v_{\mathrm{d}z}'\delta v_{\mathrm{d}z}^*),\tag{C3}$$

$$sU_3=k_xc_s^2\,\mathrm{Im}\,(W\delta v_{\mathrm{g}x}^*)-c_s^2\,\mathrm{Re}\,(W'\delta v_{\mathrm{g}z}^*),\tag{C4}$$

$$\begin{aligned}sU_4\ =\ &-\frac{\epsilon\Omega}{\mathrm{St}}\left[(v_{\mathrm{g}x}-v_{\mathrm{d}x})\mathrm{Re}(Q\delta v_{\mathrm{g}x}^*)\right.\\&+4(v_{\mathrm{g}y}-v_{\mathrm{d}y})\mathrm{Re}(Q\delta v_{\mathrm{g}y}^*)\\&+|\delta v_{\mathrm{g}x}-\delta v_{\mathrm{d}x}|^2+4|\delta v_{\mathrm{g}y}-\delta v_{\mathrm{d}y}|^2\\&\left.+|\delta v_{\mathrm{g}z}-\delta v_{\mathrm{d}z}|^2\right],\end{aligned}\tag{C5}$$

$$sU_5=\frac{\epsilon\Omega}{\mathrm{St}}v_{\mathrm{d}z}\,\mathrm{Re}\,(Q\delta v_{\mathrm{g}z}^*),\tag{C6}$$

$$sU_6=\mathrm{Re}\,(\delta F_x^{\mathrm{visc}}\delta v_{\mathrm{g}x}^*+4\delta F_y^{\mathrm{visc}}\delta v_{\mathrm{g}y}^*+\delta F_z^{\mathrm{visc}}\delta v_{\mathrm{g}z}^*),\tag{C7}$$

where $\delta\boldsymbol{F}^{\mathrm{visc}}$ is given by Equations (44)–(46).

As in the one-fluid model, we can associate U_1 with the vertical shear in the equilibrium velocities, U_2 with dust settling, U_3 with gas pressure forces, U_4 with the dust–gas relative drift, and U_5 with vertical buoyancy. The full two-fluid framework also includes viscous contributions, U_6, which is ignored in the one-fluid treatment.

ORCID iDs

Min-Kai Lin https://orcid.org/0000-0002-8597-4386

References

Adams, F. C., Ruden, S. P., & Shu, F. H. 1989, ApJ, 347, 959
Auffinger, J., & Laibe, G. 2018, MNRAS, 473, 796
Bai, X.-N., & Stone, J. M. 2010a, ApJS, 190, 297
Bai, X.-N., & Stone, J. M. 2010b, ApJ, 722, 1437
Bai, X.-N., & Stone, J. M. 2010c, ApJL, 722, L220
Balbus, S. A. 2003, ARA&A, 41, 555
Balbus, S. A., & Hawley, J. F. 1992, ApJ, 400, 610
Balsara, D. S., Tilley, D. A., Rettig, T., & Brittain, S. D. 2009, MNRAS, 397, 24
Barker, A. J., & Latter, H. N. 2015, MNRAS, 450, 21
Benítez-Llambay, P., Krapp, L., & Pessah, M. E. 2019, ApJS, 241, 25
Birnstiel, T., Fang, M., & Johansen, A. 2016, SSRv, 205, 41
Birnstiel, T., Klahr, H., & Ercolano, B. 2012, A&A, 539, A148
Blum, J. 2018, SSRv, 214, 52
Burns, K. J., Vasil, G. M., Oishi, J. S., Lecoanet, D., & Brown, B. P. 2020, PhRvR, 2, 023068
Carrera, D., Simon, J. B., Li, R., Kretke, K. A., & Klahr, H. 2020, arXiv:2008.01727
Chen, K., & Lin, M.-K. 2020, ApJ, 891, 132
Chiang, E. 2008, ApJ, 675, 1549
Chiang, E., & Youdin, A. N. 2010, AREPS, 38, 493
Dubrulle, B., Morfill, G., & Sterzik, M. 1995, Icar, 114, 237
Flock, M., Nelson, R. P., Turner, N. J., et al. 2017, ApJ, 850, 131
Garaud, P., & Lin, D. N. C. 2004, ApJ, 608, 1050
Goldreich, P., & Lynden-Bell, D. 1965, MNRAS, 130, 125
Goldreich, P., & Ward, W. R. 1973, ApJ, 183, 1051
Gole, D. A., Simon, J. B., Li, R., Youdin, A. N., & Armitage, P. J. 2020, ApJ, 904, 132
Ishitsu, N., Inutsuka, S.-I., & Sekiya, M. 2009, arXiv:0905.4404
Jacquet, E., Balbus, S., & Latter, H. 2011, MNRAS, 415, 3591
Jaupart, E., & Laibe, G. 2020, MNRAS, 492, 4591
Johansen, A., Blum, J., Tanaka, H., et al. 2014, in Protostars and Planets VI, ed. H. Beauther et al. (Tuscon, AZ: Univ. Arizona Press), 547
Johansen, A., & Youdin, A. 2007, ApJ, 662, 627
Johansen, A., Youdin, A., & Mac Low, M.-M. 2009, ApJL, 704, L75
Johnson, B. M., & Gammie, C. F. 2005, ApJ, 626, 978
Kowalik, K., Hanasz, M., Wóltański, D., & Gawryszczak, A. 2013, MNRAS, 434, 1460
Krapp, L., Benítez-Llambay, P., Gressel, O., & Pessah, M. E. 2019, ApJL, 878, L30
Krapp, L., Youdin, A. N., Kratter, K. M., & Benítez-Llambay, P. 2020, MNRAS, 497, 2715
Laibe, G., Bréhier, C.-E., & Lombart, M. 2020, MNRAS, 494, 5134
Laibe, G., & Price, D. J. 2014, MNRAS, 440, 2136
Latter, H. N., & Ogilvie, G. I. 2006, MNRAS, 372, 1829
Latter, H. N., & Papaloizou, J. 2018, MNRAS, 474, 3110
Lee, A. T., Chiang, E., Asay-Davis, X., & Barranco, J. 2010, ApJ, 718, 1367
Li, R., Youdin, A. N., & Simon, J. B. 2019, ApJ, 885, 69
Lin, M.-K. 2013, ApJ, 765, 84
Lin, M.-K. 2019, MNRAS, 485, 5221
Lin, M.-K., & Kratter, K. M. 2016, ApJ, 824, 91
Lin, M.-K., & Papaloizou, J. C. B. 2011a, MNRAS, 415, 1426
Lin, M.-K., & Papaloizou, J. C. B. 2011b, MNRAS, 415, 1445
Lin, M.-K., & Youdin, A. N. 2015, ApJ, 811, 17
Lin, M.-K., & Youdin, A. N. 2017, ApJ, 849, 129
Lovascio, F., & Paardekooper, S.-J. 2019, MNRAS, 488, 5290
Lubow, S. H., & Pringle, J. E. 1993, ApJ, 409, 360
Manger, N., Klahr, H., Kley, W., & Flock, M. 2020, MNRAS, 499, 1841
Mathis, J. S., Rumpl, W., & Nordsieck, K. H. 1977, ApJ, 217, 425
McNally, C. P., & Pessah, M. E. 2015, ApJ, 811, 121
Nakagawa, Y., Sekiya, M., & Hayashi, C. 1986, Icar, 67, 375
Nelson, R. P., Gressel, O., & Umurhan, O. M. 2013, MNRAS, 435, 2610
Nesvorný, D., Li, R., Youdin, A. N., Simon, J. B., & Grundy, W. M. 2019, NatAs, 3, 808
Paardekooper, S.-J., McNally, C. P., & Lovascio, F. 2020, MNRAS, 499, 4223
Pan, L. 2020, ApJ, 898, 8
Pan, L., & Yu, C. 2020, ApJ, 898, 7
Price, D. J., & Laibe, G. 2015, MNRAS, 451, 813
Savonije, G. J., & Heemskerk, M. H. M. 1990, A&A, 240, 191
Schäfer, U., Johansen, A., & Banerjee, R. 2020, A&A, 635, A190
Schäfer, U., Yang, C.-C., & Johansen, A. 2017, A&A, 597, A69
Schaffer, N., Yang, C.-C., & Johansen, A. 2018, A&A, 618, A75
Schreiber, A., & Klahr, H. 2018, ApJ, 861, 47
Shakura, N. I., & Sunyaev, R. A. 1973, A&A, 24, 337
Shi, J.-M., & Chiang, E. 2013, ApJ, 764, 20
Simon, J. B., Armitage, P. J., Li, R., & Youdin, A. N. 2016, ApJ, 822, 55
Squire, J., & Hopkins, P. F. 2018a, ApJL, 856, L15
Squire, J., & Hopkins, P. F. 2018b, MNRAS, 477, 5011
Squire, J., & Hopkins, P. F. 2020, MNRAS, 498, 1239
Stoll, M. H. R., & Kley, W. 2016, A&A, 594, A57
Takeuchi, T., & Lin, D. N. C. 2002, ApJ, 581, 1344
Testi, L., Birnstiel, T., Ricci, L., et al. 2014, in Protostars and Planets VI, ed. H. Beuther et al. (Tuscon, AZ: Univ. Arizona Press), 339
Tilley, D. A., Balsara, D. S., Brittain, S. D., & Rettig, T. 2010, MNRAS, 403, 211
Tominaga, R. T., Takahashi, S. Z., & Inutsuka, S.-i. 2019, ApJ, 881, 53
Umurhan, O. M., Estrada, P. R., & Cuzzi, J. N. 2020, ApJ, 895, 4
Weidenschilling, S. J. 1977, MNRAS, 180, 57
Whipple, F. L. 1972, in Proc. of the Nobel Symp. 21: From Plasma to Planet, ed. A. Elvius (New York: Wiley), 211
Yang, C.-C., & Johansen, A. 2014, ApJ, 792, 86
Yang, C. C., Johansen, A., & Carrera, D. 2017, A&A, 606, A80
Yang, C.-C., mac Low, M.-M., & Johansen, A. 2018, ApJ, 868, 27
Youdin, A., & Johansen, A. 2007, ApJ, 662, 613
Youdin, A. N. 2011, ApJ, 731, 99
Youdin, A. N., & Goodman, J. 2005, ApJ, 620, 459
Youdin, A. N., & Lithwick, Y. 2007, Icar, 192, 588
Zhu, Z., Stone, J. M., & Bai, X.-N. 2015, ApJ, 801, 81
Zhu, Z., & Yang, C.-C. 2020, MNRAS, 501, 467
Zhuravlev, V. V. 2019, MNRAS, 489, 3850
Zhuravlev, V. V. 2020, MNRAS, 494, 1395